

**Investigating the Impact of Using CFD generated Unsteady Mach
Number Dynamic Stall Data for Numerical Rotor Analysis of
Helicopter Forward Flight**

by

**Dustin Jee
B.Eng.**

A thesis submitted to the Faculty of Graduate and Postdoctoral Affairs in partial
fulfillment of the requirements for the degree of

**Master of Applied Science
in
Aerospace Engineering**

Ottawa-Carleton Institute for Mechanical and Aerospace Engineering
Department of Mechanical and Aerospace Engineering
Carleton University
Ottawa, Ontario
August, 2017

Copyright © 2017

Dustin Jee

Abstract

When the rotor blades are at a high advance ratio and/or a high thrust coefficient, the onset of dynamic stall makes accurate prediction of airloads on the rotor blades difficult. Comprehensive rotor analysis codes used in the industry rely on semi-empirical dynamic stall models to generate the aerodynamic coefficients of the blade sections undergoing dynamic stall. However, these models neglect the unsteady nature of the freestream seen by the blade sections compromising the accuracy of the analysis at high speed forward flight and high blade loading conditions. Thus, this thesis aims to investigate the impact of including the unsteady freestream effects in dynamic stall for the prediction of the airloads on the rotor blades.

To study the impact of including the unsteady nature of the freestream in dynamic stall, Computational Fluid Dynamics (CFD) was used to generate the unsteady 2D dynamic stall aerodynamic data. The CFD data then served as inputs to the in-house rotor analysis code called *Qoptr* to generate blade airload results. The flight test data from a steady-level flight case ($C_T/\sigma = 0.129$, $\mu = 0.24$) from the UH-60A Airloads program was used for validation. The *Qoptr* blade airload results generated with the unsteady CFD dynamic stall data showed considerably better agreement with the flight test data than the results generated with semi-empirical dynamic stall models, especially in the sectional moment results.

Acknowledgements

I would like to first thank my family for their unconditional support throughout the course of this work. They were my biggest motivator from day one, and this work would not have been possible without them.

I also must thank my thesis supervisor Dr. Daniel Feszty for providing and administering this exciting research and professional development opportunities. His continuous encouragement and guidance since my undergraduate years brought me to where I am today. Also, sincere thanks to Professor Nitzsche for his co-supervision and overlooking the last stages of this work.

Sincere thanks to former and current students of the Carleton rotorcraft research group for all their help, especially Daniel Gosselin, Jonathan Wiebe, and Khider Al-Jaburi for their help in the early stages of this work.

Lastly, I would like to thank the Natural Sciences and Engineering Research Council of Canada (NSERC) and the government of Ontario for their financial support.

Table of Contents

Abstract	ii
Acknowledgements	iii
Table of Contents	iv
List of Tables	viii
List of Figures	ix
Nomenclature	xiii
Chapter 1: Introduction	1
1.1 Helicopter Aerodynamics	1
1.1.1 Hovering Flight	2
1.1.2 Forward Flight.....	3
1.2 Static Stall and Dynamic Stall	4
1.2.1 Static Stall	4
1.2.2 Dynamic Stall.....	6
1.2.2.1 Flow Morphology of Dynamic Stall	7
1.2.2.2 Dynamic Stall in the Rotor Environment.....	9
1.2.2.3 Current Industry Practice of Accounting for Dynamic Stall.....	10

1.3	Thesis Objectives.....	11
Chapter 2: Background and Literature Review		12
2.1	Dynamic Stall: State of the Art.....	12
2.1.1	Modelling Constant Freestream Dynamic Stall in CFD	12
2.1.2	Time-Varying (unsteady) Freestream Dynamic Stall	16
2.2	Rotorcraft Comprehensive Analysis.....	18
2.2.1	A Brief History of Rotorcraft Comprehensive Analysis	18
2.2.2	Dynamic Stall Handling in Rotorcraft Comprehensive Analyses.....	19
2.2.2.1	Semi-Empirical Dynamic Stall Models.....	19
2.3	UH-60A Airloads Program.....	21
2.3.1	Counter 9017 Case from UH-60A Airloads Program.....	22
2.3.2	Semi-empirical Dynamic Stall Model Validation.....	23
Chapter 3: Numerical Methods		26
3.1	Qoptr (Rotor analysis code).....	26
3.1.1	Blade and Azimuth Discretization Dependence Study	27
3.1.2	Input Parameters to Qoptr	28
3.2	Computational Fluid Dynamics (CFD)	31
3.2.1	Quasi-steady Case	31
3.2.1.1	Computational Domain and Boundary Conditions	31
3.2.1.2	Shockwave Capturing	34

3.2.1.3	CFD Validation	35
3.2.2	Constant Freestream Dynamic Stall Case	36
3.2.2.1	Computational Domain and Boundary Conditions	36
3.2.2.2	Initial Conditions.....	38
3.2.2.3	Angle of Attack Oscillation.....	39
3.2.2.4	Cycle Periodicity Convergence	39
3.2.2.5	Verification and Validation.....	40
3.2.3	Time-varying Freestream Dynamic Stall Case	42
3.2.3.1	Fluctuating Velocity Inlet Condition.....	42
3.2.3.2	Verification.....	43
3.2.3.3	Application of Time Lag.....	44
3.2.3.4	Cycle Periodicity Convergence	45
3.3	Utilization of Dynamic Stall Aerodynamic Data in Qoptr	46
3.3.1	Characteristics of Dynamic Stall Aerodynamic Data	46
3.3.2	Aerodynamic Data Look-up Table Organization in Qoptr	47
3.3.2.1	Data Selection in Hover Analysis	47
3.3.2.2	Data Selection in Forward Flight Analysis	48
Chapter 4: Results.....		50
4.1	Effects of Mach Number on Dynamic Stall	50
4.1.1	Effects of Mach Number on Constant Freestream Dynamic Stall	50

4.2	Effects of Unsteady Freestream on Dynamic Stall.....	53
4.3	Effects of Angle of Attack Range on Unsteady Freestream Dynamic Stall.....	54
4.4	Qoptr Results with Constant Freestream CFD Dynamic Stall Data.....	55
4.5	Qoptr Results with Unsteady Freestream CFD Dynamic Stall Data.....	58
4.5.1	Factors Influencing Solution Accuracy.....	60
4.5.2	Blade Airload Results at Other Radial Positions	63
Chapter 5: Conclusions and Recommendations		68
5.1	Conclusions and Accomplishments.....	68
5.2	Recommendations for Future Work	69
References.....		70
Appendix A: Fluent Input Files.....		76
Appendix B: Blade Geometry Used in Qoptr.....		84

List of Tables

Table 1.1: Five stages of dynamic stall process.	8
Table 2.1: Summary of time-varying freestream dynamic stall studies [16].	16
Table 2.2: Counter 9017 description.	22
Table 3.1: Discretization dependence study for forward flight analysis for Counter 9017 at $C_T/\sigma = 0.129$, $\mu = 0.24$	28
Table 3.2: Rotor parameters used in Qoptr for UH-60A.	29
Table 3.3: Main simulation parameters.	34
Table 3.4: Summary of simulation parameters for constant freestream case.	37
Table 3.5: Validation case test conditions.	40

List of Figures

Figure 1.1: Top view of rotor plane in hovering flight, adapted from Ref. [1]	2
Figure 1.2: Top view of rotor plane in forward flight, adapted from Ref. [1].	3
Figure 1.3: Illustration of typical static stall.	6
Figure 1.4: Visual representation of static stall mechanisms [3].	6
Figure 1.5: Schematic representation of stages of dynamic stall. (a) Appearance of flow reversal. (b) LE flow separation. (c) LEV convects aft. (d) Full separation. (e) Flow reattachment. Adapted from [1].	8
Figure 1.6: (a) Dynamic stall rotor map for steady-level flight at $\mu = 0.237$ and $n_z = 1.01$. (b) Dynamic stall rotor map for pull-up maneuver at $\mu = 0.329$ and $n_z = 2.11$	10
Figure 2.1: Constant freestream dynamic stall aerodynamic coefficient validation on EDI-M109 and OA209 airfoils at $M = 0.3, Re = 1.16 \times 10^6, \alpha = 13^\circ \pm 7^\circ, k = 0.05$ [14].	14
Figure 2.2: Validation of results with (a) S-A and (b), $k - \omega$ SST turbulence models with NACA 0012 $M = 0.3, Re = 3.76 \times 10^6, \alpha = 15^\circ \pm 10^\circ$ [13].	15
Figure 2.3: Comparison of experimental dynamic stall data to results computed with L-B and ONERA EDLIN model on SC1095 airfoil at $M = 0.301, Re = 3.98 \times 10^6, \alpha = 11.86^\circ \pm 7.9^\circ$, experimental data from Ref. [11].	20

Figure 2.4: Comparison of experimental dynamic stall data to results computed with L-B and ONERA EDLIN model on NACA0012 airfoil at $M = 0.301$, $Re = 3.98 \times 10^6$, $\alpha = 11.86^\circ \pm 7.9^\circ$, experimental data from Ref. [11].	20
Figure 2.5: Dynamic stall rotor map for Counter 9017 [6].	22
Figure 2.6: Comparison of flight test data with computed results using dynamic stall models (adapted from Ref. [8]).	24
Figure 3.1: UH-60A blade geometry (a) blade twist and (b) airfoil distribution [46].	29
Figure 3.2: Airfoils on UH-60A rotor blade (a) SC1095 and (b) SC1094 R8 [46].	29
Figure 3.3: Validation of Qoptr hover results (a) figure of merit and (b) power coefficient.	30
Figure 3.4: Effect of far-field distance on lift coefficient of NACA 0012 at $M = 0.8$ and $\alpha = 1.25^\circ$. [15].	32
Figure 3.5: Full view of computational domain.	32
Figure 3.6: Computational domain (a) refined region around airfoil and (b) inflation layers in boundary layer.	33
Figure 3.7: Verification of high Mach number flow condition.	34
Figure 3.8: High Mach number case validation with NACA0012 at $M=0.7$, $Re=9 \times 10^6$, and $\alpha=1.49^\circ$ (Experimental data from Ref. [41]).	35
Figure 3.9: Low Mach number case validation with SC1095 at $M=0.3$, $Re=3.88 \times 10^6$, and $\alpha=13.5^\circ$ (Experimental data from Ref. [11]).	36
Figure 3.10: Circular domain around the airfoil.	38
Figure 3.11: A sample angle of attack variation as a function of blade azimuth for constant freestream case.	39
Figure 3.12: Time history of aerodynamic loads.	40

Figure 3.13: Grid dependence test for constant freestream case.....	41
Figure 3.14: Comparison of CFD data to experimental data for constant freestream dynamic stall case.....	41
Figure 3.15: A sample angle of attack and inlet velocity variation as a function of blade azimuth for unsteady freestream case.	43
Figure 3.16: Grid dependence study for unsteady freestream dynamic stall case at $M = 0.53 \pm 0.16$ and $\alpha = 8^\circ \pm 8^\circ$	44
Figure 3.17: Application of time lag for unsteady freestream case.	45
Figure 3.18: Time history of aerodynamic loads for unsteady freestream case.	46
Figure 3.19: Hysteretic aerodynamic behaviour of dynamic stall on NACA 0012 (Adapted from Ref. [1]).....	47
Figure 3.20: Blade angle of attack stroke phase.	48
Figure 3.21: Aerodynamic data selection and assignment flowchart.	49
Figure 4.1: Effect of Mach number of constant freestream dynamic stall on SC1094 airfoil.	51
Figure 4.2: Mach number contour of SC1094 R8 airfoil at $M = 0.4$ and $\alpha = 11^\circ$	51
Figure 4.3: Mach number contour of SC1094 airfoil at $M = 0.5$ and $\alpha = 11^\circ$	52
Figure 4.4: Mach number contour of SC1094 R8 airfoil at $M = 0.6$ and $\alpha = 11^\circ$	52
Figure 4.5: Comparison of lift coefficient from steady and unsteady freestream dynamic stall.	53
Figure 4.6: Comparison of moment coefficient from steady and unsteady freestream dynamic stall.	53
Figure 4.7: Effect of AOA range on variable freestream dynamic stall behavior on SC1094R8 airfoil.....	54

Figure 4.8: Comparison of constant freestream CFD dynamic stall data to semi-empirical dynamic stall model results.	56
Figure 4.9: Comparison of constant freestream DS Qoptr results to flight test data.	57
Figure 4.10: Comparison of unsteady freestream DS Qoptr results to flight test data.	59
Figure 4.11: Effect of angle of attack range sensitivity on solution accuracy.	61
Figure 4.12: Airload prediction error in full 3D CFD rotor simulation [43].	62
Figure 4.13: Separation bubble formation during down-stroke phase.	63
Figure 4.14: Qoptr blade airload results at $r/R = 0.675$	65
Figure 4.15: Qoptr blade airload results at $r/R = 0.865$	66

Nomenclature

Symbol	Definition [units]
a	Speed of sound [m/s]
A	Rotor disk area [m ²]
c	Airfoil chord length [m]
C_d	Section drag coefficient [-]
C_l	Section lift coefficient [-]
C_m	Section moment coefficient [-]
C_p	Rotor power coefficient [-]
C_T	Rotor thrust coefficient [-]
I	Turbulence intensity [-]
k	Reduced frequency [-]
M	Mach number [-]
n	Load factor [-]
r/R	Rotor radial position [-]
R	Rotor radius [m]

Re	Reynolds number [-]
t	time [s]
T	Rotor thrust [N]
U	Velocity [m/s]
α	Angle of attack [deg]
μ	Advance ratio [-]
ρ	Density [kg/m ³]
ψ	Blade azimuth [deg]
ω	Angular velocity [rad/s]

Abbreviations

Definition

AOA	Angle of Attack
BEMT	Blade Element Momentum Theory
BVI	Blade Vortex Interaction
CAMRAD	Comprehensive Analytical Model of Rotorcraft Aerodynamics and Dynamics
CFD	Computational Fluid Dynamics
CSD	Computational Structural Dynamics
LEV	Leading Edge Vortex
LSB	Laminar Separation Bubble

NASA National Aeronautics and Space Administration

SST Shear Stress Transport

S-A Spalart-Allmaras

TEV Trailing Edge Vortex

Chapter 1

Introduction

Due to their unique capability to take off and land vertically on various types of terrain, helicopters are widely used for military, search and rescue, and civilian applications. This capability also gives rise to phenomena and design challenges that are unique to helicopters. Occurrence of dynamic stall on helicopter rotors is one of these phenomena and the prediction of the blade loads associated with it is a major design challenge. This chapter describes the general flight regimes of helicopter flight with their respective rotor mechanics, the phenomenon of dynamic stall and its effect, and introduces the objective of this thesis.

1.1 Helicopter Aerodynamics

In contrast to fixed-wing aircraft where lift and thrust are generated independently, both the lift and the propulsive force of a helicopter are generated by the main rotor. Thus, as the helicopter goes through different flight regimes during the course of its mission, the parameters of the main rotor also change accordingly. Due to its dynamic role, the main rotors of helicopters are complex systems whose design requires multi-objective optimization.

The two main flight regimes that take precedence in the design process are hovering and forward flight, as most time is spent in these regimes during typical missions served by helicopters. There are several configurations of helicopters, mainly differing in how the torque generated by the main rotor(s) is counteracted and how yaw control is achieved. In this thesis, the single main rotor and

single tail rotor configuration is considered for the description of helicopter aerodynamics as it is the most common configuration.

1.1.1 Hovering Flight

In hovering flight, the angle of attack of the rotor blades is constant throughout the blade azimuth. The velocity of the freestream along the rotor blades is also constant throughout the blade azimuth as shown in Figure 1.1. Therefore, the aerodynamics of the rotor blades in hovering flight can be considered quasi-steady.

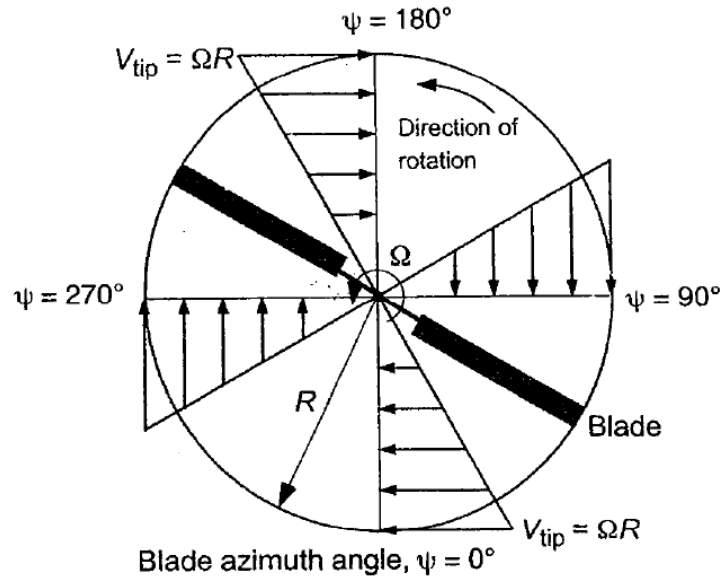


Figure 1.1: Top view of rotor plane in hovering flight, adapted from Ref. [1].

Without any incoming freestream, the velocity of the airflow over a blade section caused by the rotating motion can be calculated as the following.

$$U_{rotation} = r\Omega \quad (1.1)$$

1.1.2 Forward Flight

In forward flight, the oncoming freestream introduces complexity to the aerodynamics of the rotor blades. At a forward flight speed of U_∞ , a component of velocity that varies as a function of blade azimuth can be represented as:

$$U_{forward} = U_\infty \sin(\psi) \quad (1.2)$$

Then, the resultant velocity of the airflow over a blade section in forward flight can be obtained by summing Equations (1.1) and (1.2) as seen in Figure 1.2.

$$U = U_{rotation} + U_{forward} \quad (1.3)$$

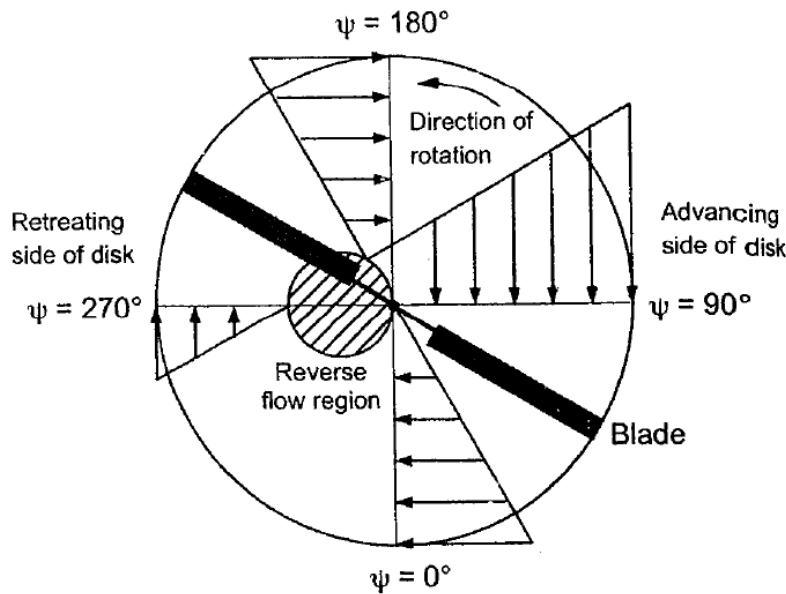


Figure 1.2: Top view of rotor plane in forward flight, adapted from Ref. [1].

The forward flight speed of a helicopter is often expressed by a dimensionless quantity known as “advance ratio”, denoted as μ . Advance ratio is a ratio of the helicopter’s forward flight speed to the blade tip speed.

$$\mu = \frac{U_\infty}{U_{TIP}} = \frac{U_\infty}{R\Omega} \quad (1.4)$$

Advance ratio also describes the size of the reverse flow region on the rotor blade in forward flight as indicated in Figure 2.2. In fact, the diameter of this region is exactly equal to the product of advance ratio and rotor radius. Helicopters typically cruise at advance ratios ranging from 0.2 to 0.3, meaning that 20 to 30% of the rotor blade does not generate any lift near the 270° blade azimuth. The complex flow phenomena that appear at high advance ratios are responsible for its low flight speed in comparison to that of its fixed-wing counterparts. At high advance ratios, the retreating blade experiences reverse flow on the inboard region and stall on the outboard region, while the advancing blade sees shock waves induced by transonic airflow near the blade tip. Under these conditions, the significant increase in aerodynamic loads on the rotor blades causes excess torsional blade loading and blade vibration. These adverse aerodynamic phenomena at high advance ratios are discussed in more detail in the following sections.

1.2 Static Stall and Dynamic Stall

In aerodynamics, stall refers to a condition where the boundary layer separates from the upper surface of the lifting surface, causing a decrease in lift generated by the surface. Stall occurs when the angle of attack of the wing exceeds a certain angle, known as the critical angle or stall angle. This angle varies widely depending on the shape of the lifting surface, the Reynolds number, and the Mach number of the freestream. In the following sections, the mechanics of static and dynamic stall are described in detail.

1.2.1 Static Stall

On a typical airfoil, the lift increases linearly as the angle of attack is increased until it reaches the stall angle. Once the stall angle is reached, the lift starts to decrease. This decrease in lift is not

abrupt on most airfoils used for lift surfaces of aircraft to give pilots time to recover in the event of stall. Figure 1.3 shows a typical lift curve of an airfoil undergoing static stall, and Figure 1.4 shows a visual representation of the stall mechanisms discussed for the three types of static stall. Depending on the shape of the airfoil and the freestream conditions, static stall can occur in one of three ways: trailing-edge stall, leading-edge stall, and thin airfoil stall [2]. The trailing-edge stall, perhaps the most well known type of stall, occurs when turbulent separation moves forward from the trailing edge toward the leading edge with increasing angle of attack. Turbulent separation occurs at the trailing edge as soon as the maximum lift is obtained. The forward progression of turbulent separation is gradual and continual. This type of stall is inherent to airfoils with large thickness. Seen on airfoils with moderate thickness, leading-edge stall occurs when a strong adverse pressure gradient causes laminar boundary layer separation at low angles of attack. The boundary layer may reattach as the flow transitions to turbulent flow, forming a laminar separation bubble. As the angle of attack increases, the laminar separation bubble moves toward the leading edge until the stall angle is reached at which point reattachment is no longer possible. Compared to the trailing-edge stall, leading-edge stall is more abrupt as the entirety of the boundary layer separates at once. As the name indicates, the third and last type of static stall thin airfoil stall occurs on sharp-edge airfoils. As the angle of attack increases, the reattachment point moves aft after the formation of a laminar separation bubble. Stall occurs when the separation bubble bursts and fails to reattach.

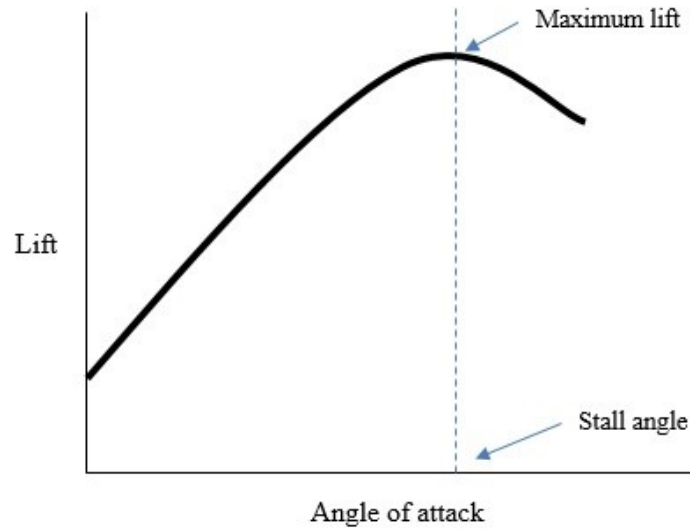


Figure 1.3: Illustration of typical static stall.

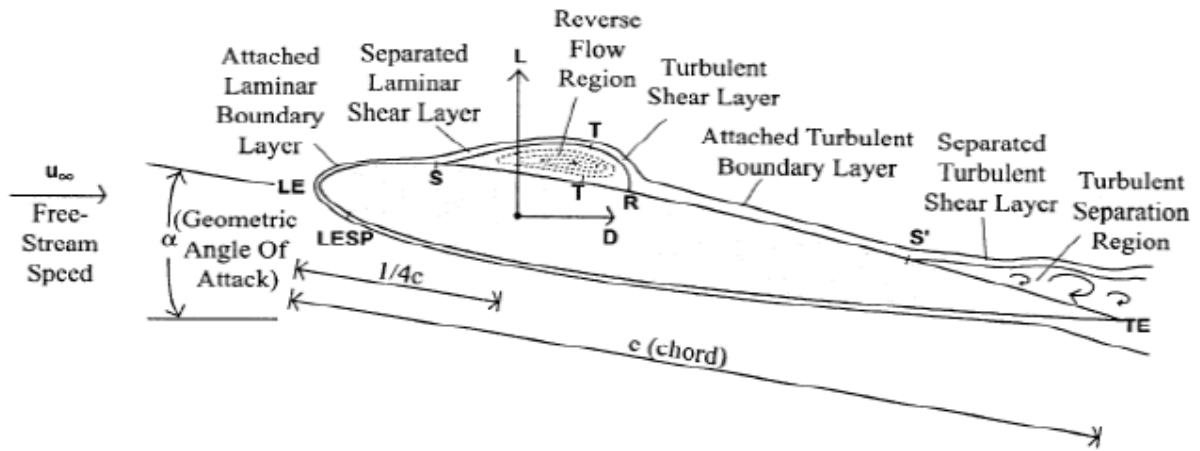


Figure 1.4: Visual representation of static stall mechanisms [3].

1.2.2 Dynamic Stall

Dynamic stall can occur when the change in angle of attack is rapid. A non-dimensional parameter known as the *reduced frequency* is used to characterize the degree of unsteadiness of the pitching motion [1].

$$k = \frac{\omega c}{2U} \quad (1.5)$$

Interestingly, this non-dimensional parameter appears when non-dimensionalizing the Navier-Stokes equations. Moreover, the force on an oscillating airfoil is a function of the reduced frequency along with the Mach number and Reynolds number. At reduced frequencies greater 0.05, the flow is considered unsteady, and dynamic stall may take place. In typical helicopter forward flight, the reduced frequency is between 0.05 and 0.1 on the outboard region of the rotor blade.

1.2.2.1 Flow Morphology of Dynamic Stall

The phenomena of dynamic stall have been studied mainly through oscillating wind tunnel experiments [1]. Works of McCroskey [4], and Beddoes [5] provide a detailed description of the dynamic stall flow morphology in the perspective of unsteady airfoil theory. In this section, the key characteristics of the dynamic stall flow morphology are described with a focus on the effect of maximum angle of attack reached.

The dynamic stall process can be divided into five stages. Table 1.1 summarizes the five stages as suggested by Leishman [1]. Schematic representation of the corresponding flow field can be seen in Figure 1.5.

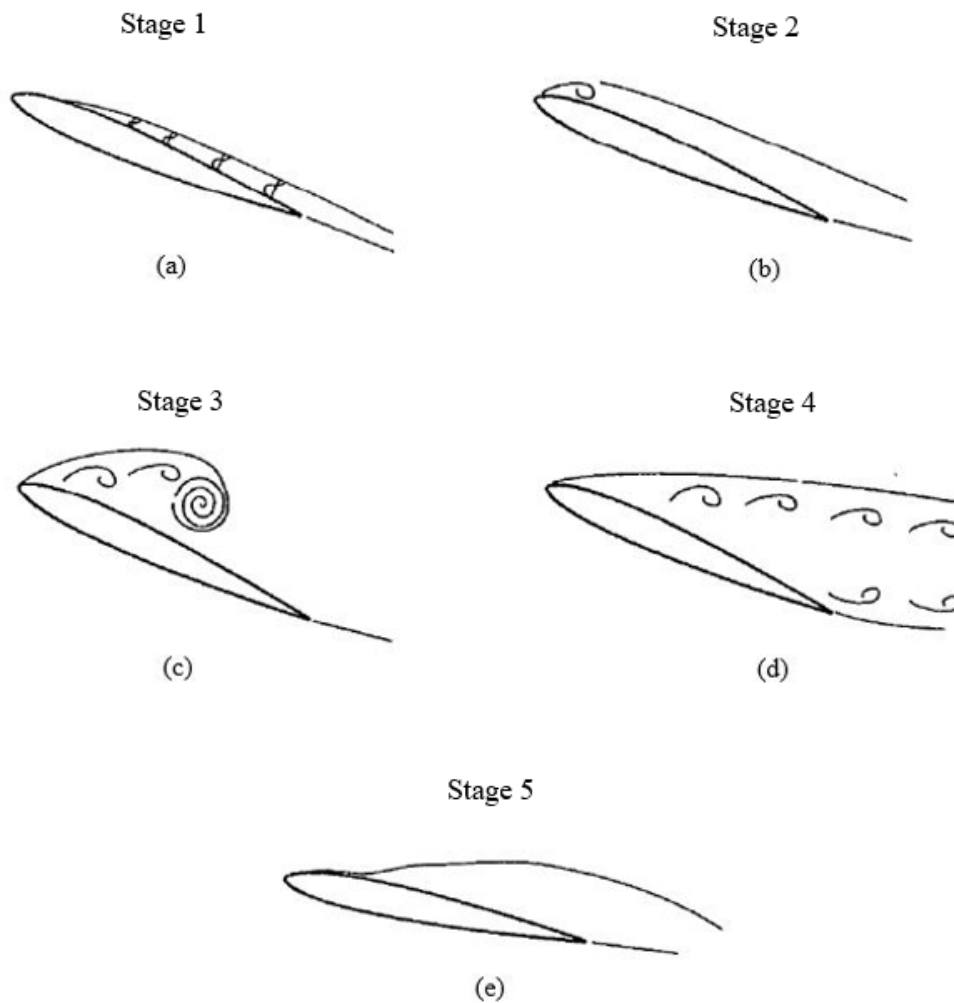


Figure 1.5: Schematic representation of stages of dynamic stall. (a) Appearance of flow reversal. (b) LE flow separation. (c) LEV convects aft. (d) Full separation. (e) Flow reattachment (adapted from Ref. [1]).

Table 1.1: Five stages of dynamic stall process.

Stage	Description
1	The static stall angle is exceeded and flow reversal starts to form in the boundary layer.
2	The flow separates from the upper surface of the airfoil causing moment stall.
3	Leading edge vortices (LEV) are formed and convect aft inducing extra lift.

4	The leading edge vortices reach the trailing edge. The flow is fully separated and lift stall occurs.
5	The angle of attack is lowered in the down stroke phase, and the flow reattached from front to back.

1.2.2.2 Dynamic Stall in the Rotor Environment

Dynamic stall occurs on the rotor blades when the blades are at a high advance ratio and/or high thrust coefficient, C_T . The thrust coefficient is defined as

$$C_T = \frac{T}{\rho A (\Omega R)^2} \quad (1.6)$$

where T is thrust, ρ is the density of atmospheric air, and A is the rotor disk area. At high advance ratios, the flow velocity on the retreating blade is decreased as indicated by Eq. 1.3, which requires the blade to have a higher angle of attack to generate the necessary lift. In high blade loading conditions such as turn and pull-up maneuvers, the flow velocity on the retreating blade may not be decreased significantly, but larger angles of attack are required along the blade to compensate for the increased load. Figure 1.5 shows the dynamic stall rotor maps for a UH-60A helicopter presented by Bousman [6] for a) steady-level flight, and b) high blade loading pull-up maneuver.

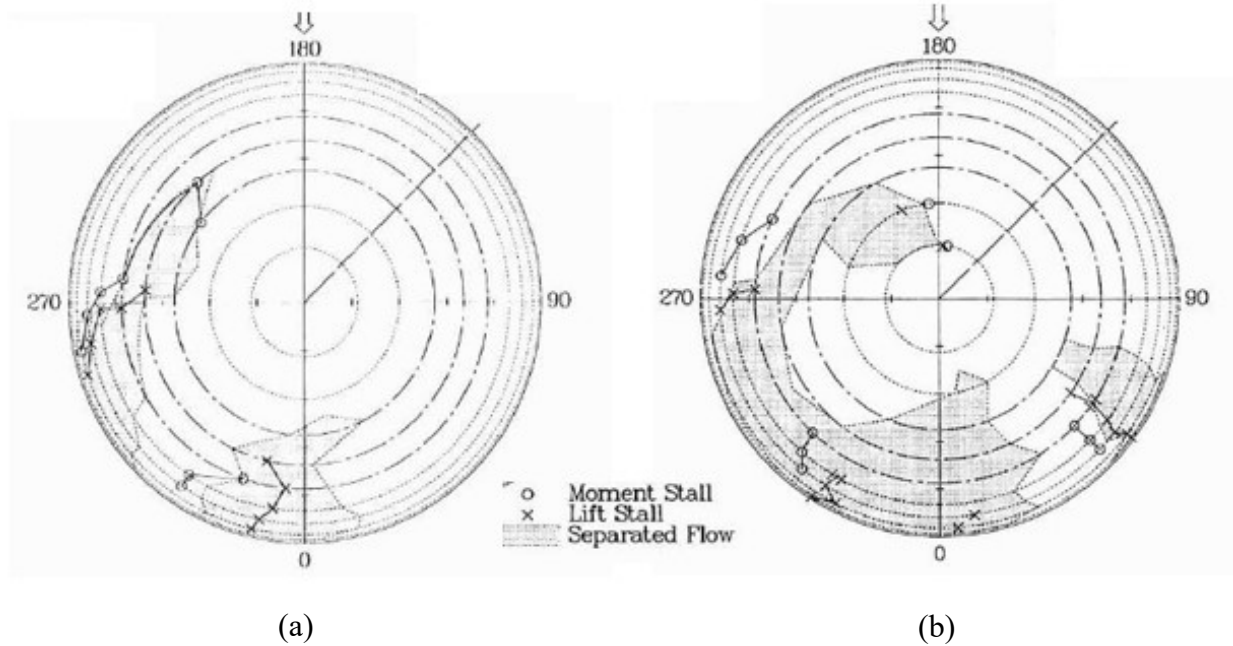


Figure 1.6: (a) Dynamic stall rotor map for steady-level flight at $\mu = 0.237$ and $n_z = 1.01$. (b) Dynamic stall rotor map for pull-up maneuver at $\mu = 0.329$ and $n_z = 2.11$ (adapted from Ref. [6]).

1.2.2.3 Current Industry Practice of Accounting for Dynamic Stall

For the design and performance analysis of helicopters, helicopter manufacturers use comprehensive rotor analysis codes to predict the aeromechanical behaviour of the rotor [7]. Aerodynamic coefficients of the rotor blades are an important input to these codes, calling for reliable dynamic stall data of the rotor blades for accurate analysis of forward flight. Currently, semi-empirical dynamic stall models [7] are often used to quickly generate the necessary aerodynamic data, but these models neglect the unsteady nature of the freestream velocity. A comparison of the results predicted by the rotor analysis codes to the flight test data shows that the accuracy of the forward flight performance prediction is less reliable than the hovering flight performance prediction which does not require dynamic stall data [8]. While other complications associated with forward flight might be partly responsible for the difficulties in forward flight

performance prediction, the differences between dynamic stall data obtained at constant freestream and time-varying or unsteady freestream suggests that the current practice of neglecting the unsteady nature of the freestream may be an important factor.

1.3 Thesis Objectives

The main objective of this work is to investigate the impact of using dynamic stall data obtained at time-varying freestream on the accuracy of forward flight blade airload prediction. The time-varying freestream dynamic stall data will be generated via computational fluid dynamics (CFD), and an in-house rotor analysis code, *Qopttr*, will be used for the prediction of the airloads on the rotor blades. The impact of using unsteady dynamic stall data will be determined by comparing the numerical data to the flight test data from the UH-60A Airloads Program headed by NASA and the U.S. Army. The comparison of the numerical data to the UH-60A flight test data will focus on qualitative correlation of the two data sets to accommodate the absence of error estimation of the flight test data.

Chapter 2

Background and Literature Review

The first section of this chapter provides a more detailed theoretical background on dynamic stall and the state of the art in dynamic stall modelling currently used in helicopter rotor analysis. The following sections outline a brief history of comprehensive rotor analysis methods, and introduce the UH-60A Airloads Program from which the validation data is obtained. Lastly, the current capabilities of rotor analysis codes are presented by means of comparing the results generated by the codes to the flight test data from the UH-60A Airloads Program.

2.1 Dynamic Stall: State of the Art

The phenomenon of dynamic stall has been recognized as a limiting factor on helicopter performance for quite some time. Works of Tarzanin [9] and McCroskey et al. [10] show that excessive blade loading and vibration caused by dynamic stall had been identified and researched on since the 1970s. Since then, significant research continued to be conducted as rotary wing technology advanced.

In the early stages of research, wind tunnel testing was primarily used to study the airloads generated on various airfoil sections. A NASA technical report [11] published in 1982 contains experimentally obtained airloads data for rotor airfoil sections at various flow conditions. As the use of CFD grows with increasing computing power, the experimental data from this technical report serves an important role in validating the data obtained via CFD.

2.1.1 Modelling Constant Freestream Dynamic Stall in CFD

With recent advances in computing technologies, dynamic stall studies via CFD have become more practical and now are a popular method of dynamic stall investigation for many researchers,

for example, Richter and Gardner [12], and Al-Jaburi [13]. From mesh generation to turbulence model studies, various aspects of dynamic stall modelling have been researched in the past decade. Most notably, the works of Richter et al. [12], [14] have established the most comprehensive CFD methodology for computing the aerodynamic behaviour of 2D airfoils undergoing constant freestream dynamic stall.

In their study, Richter et al. used a block-structured C-grid with a far-field boundary of 50 chord lengths resulting in 152,640 cells. Local refinements were applied near the leading and trailing edges of the airfoil and in the wake region. The mesh around the surface of the airfoil was refined to maintain $y^+ \sim O(1)$. Three different turbulence models, $k - \omega$ Shear Stress Transport (SST) model, two-equation Reynolds stress model (RSM), and Spalart-Allmaras (S-A) model were tested. Comparing the CFD data to the wind tunnel data showed that while the SST and RSM turbulence models performed very similarly, the S-A model showed overpredicted oscillations and early lift and moment breakdowns [14]. Figure 2.1 shows the comparison of the CFD data generated with the SST turbulence model and with the mesh described above to the experimental data gathered in the transonic wind tunnel Göttingen of the German-Dutch Wind Tunnels (DNW-TWG) for the EDI-M109 and OA209 airfoils as reported by Richter et al.

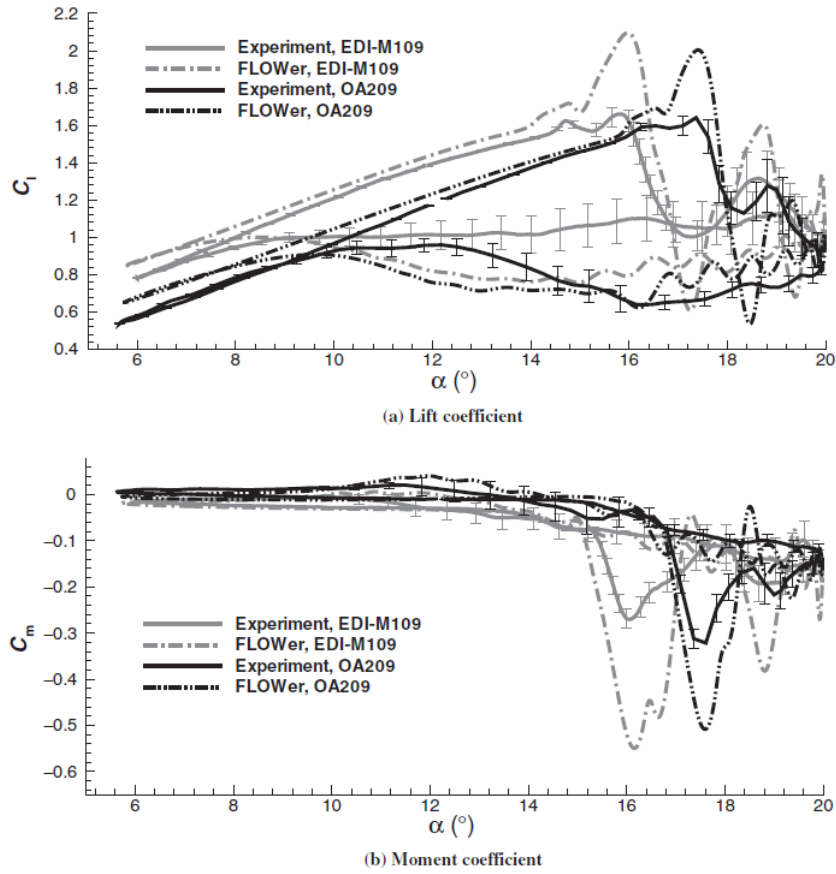


Figure 2.1: Constant freestream dynamic stall aerodynamic coefficient validation on EDI-M109 and OA209 airfoils at $M = 0.3$, $Re = 1.16 \times 10^6$, $\alpha = 13^\circ \pm 7^\circ$, $k = 0.05$ [14].

More recently, Al-Jaburi et al. [13] developed a similar methodology for simulating constant freestream dynamic stall with a commercial CFD code - ANSYS Fluent. In his methodology, Al-Jaburi uses a large computational domain with a far-field boundary of 500 chord lengths, negating any potential needs of vortex correction as recommended by Blazek [15]. Similar to the work of Richter et al., Al-Jaburi uses fine local refinement in the wake region to capture the vortex shedding. The region directly above the upper surface of the airfoil is also refined to capture shock waves in high Mach number applications. The oscillating motion of the airfoil is achieved by a sliding mesh technique. This technique involves no mesh deformation, as an interface is used to define two domains that move relative to each other rather than deforming individual cells. Maintaining the

originally intended mesh density around the airfoil is especially important for dynamic stall simulations to capture vortex shedding at high angles of attack.

Al-Jaburi validated his CFD results with experimental data from Ref. [11] with, $k - \omega$ SST and S-A turbulence models. Results obtained with the S-A turbulence model and SST turbulence model are shown in Figure 2.2 (a) and (b), respectively.

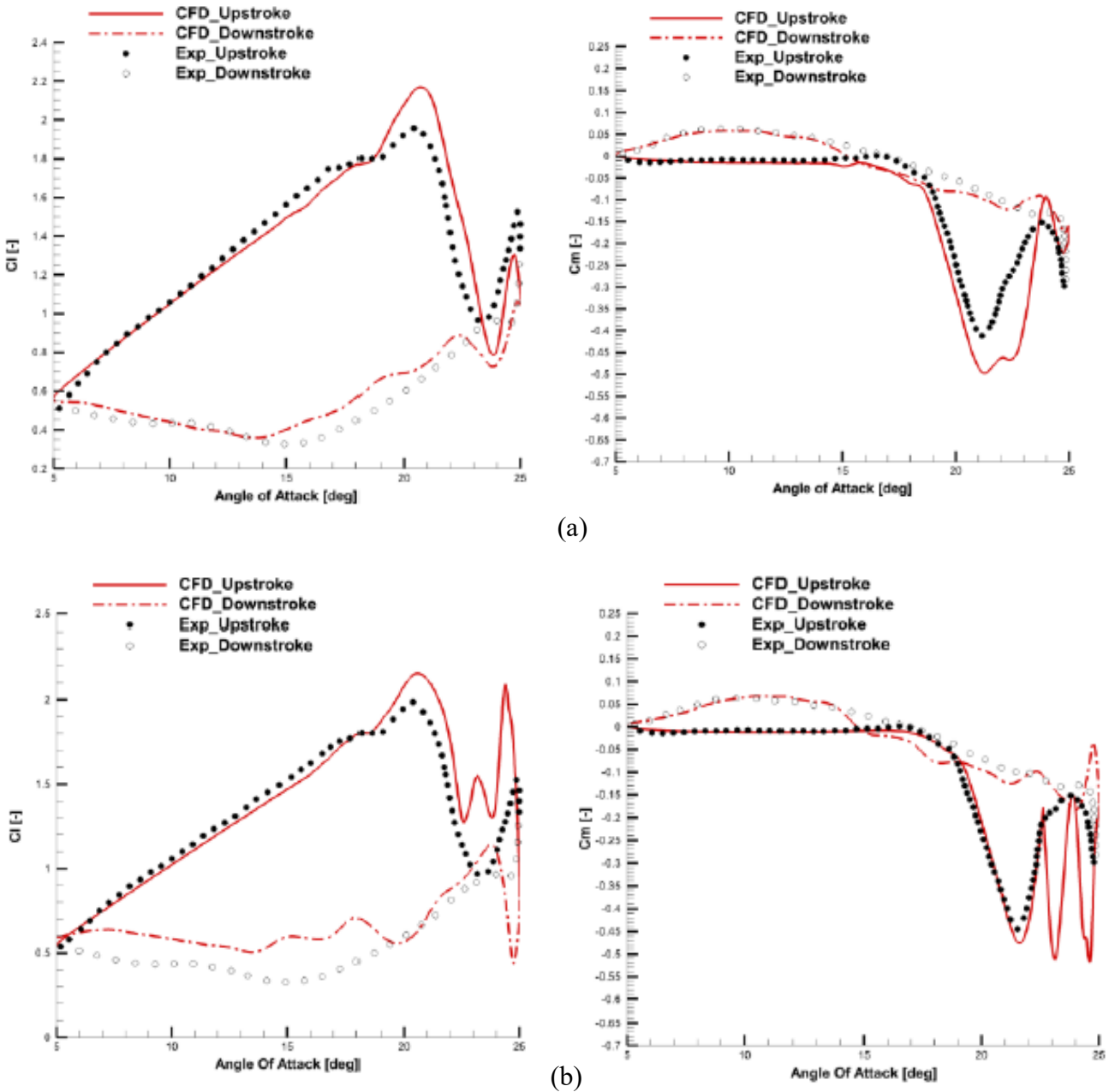


Figure 2.2: Validation of results with (a) S-A and (b), $k - \omega$ SST turbulence models with NACA 0012 at $M = 0.3, Re = 3.76 \times 10^6, \alpha = 15^\circ \pm 10^\circ$ [13].

In the results reported by Al-Jaburi et al., the performance of the turbulence models is different from what Richter et al. observed in their results. Richter et al. observed that the $k - \omega$ SST turbulence model yielded better overall accuracy than the S-A model. However, the results reported by Al-Jaburi et al. showed that the S-A turbulence model captured the overall accuracy better. The inconsistency seen in the performance of the turbulence models in these studies suggests that the performance of the turbulence models may depend on various factors such as the flow conditions, reduced frequency of the airfoil, and airfoil shape. Al-Jaburi's method was adopted for conducting steady freestream dynamic stall simulations.

2.1.2 Time-Varying (unsteady) Freestream Dynamic Stall

As seen in Table 2.1 summarized by Gosselin [16], much of the studies on time-varying freestream dynamic stall have been done experimentally at low Mach numbers. The difficulties in achieving high amplitude and high frequency Mach number fluctuations in a wind tunnel limited these studies to low Mach numbers that are much lower than the Mach numbers seen in helicopter forward flight. The stall behaviour of airfoils is largely dependent on the freestream Mach number. Therefore, a few studies have utilized CFD to employ higher Mach numbers that are representative of real helicopter forward flight conditions.

Table 2.1: Summary of time-varying freestream dynamic stall studies [16].

Reference	Type of Study	Mach Number Range	AOA Range [deg]
Pierce et al. [17]	Experimental	0.031 – 0.044	6, 10 14 ± 4 18 ± 4
Maresca et al. [18]	Experimental	0.007 – 0.058	15 ± 10 20 ± 17
Brendel and Mueller [19]	Experimental	0.013 – 0.015	-5, 0, 7
Favier et al. [20]	Experimental	0.007 – 0.058	6 ± 6 12 ± 6
Ellsworth and Mueller [21]	Experimental	3.9×10^{-5} - 4.4×10^{-5}	7
Favier et al. [22]	Experimental & Numerical	0.007 – 0.072	9 ± 6 12 ± 6

Shi and Ming [23]	Experimental	0.017 – 0.052	0 – 30, 0 – 60, 15 – 45, 30 – 60
Shi and Ming [24]	Experimental	0.012 – 0.040	0 – 60
Gompertz et al. [25]	Experimental	0.38 – 0.48	8 – 20
Kerstens and Williams [26]	Experimental	0.008 – 0.032	0 – 20
Kerho [27]	Numerical	0.34 – 0.76	10 ± 10
Martinat et al. [28]	Numerical	0.011 – 0.018	12 ± 6
Gharali and Johnson [29]	Numerical	0.009 – 0.078	10 ± 15
Gosselin et al. [16]	Numerical	0.18-0.78	15 ± 10

Kerho [27] investigated the effects of out-of-phase time-varying Mach number on dynamic stall on 2D airfoils by deriving the angle of attack and Mach number histories within one revolution for a blade section of the UH-60A helicopter from CAMRAD II and simulating these conditions in CFD. He observed notable differences between the aerodynamic coefficients generated at steady Mach number and at time-varying Mach number. Kerho observed non-linear variation in C_l in the up-stroke phase (i.e. angle of attack is increasing) and a higher $C_{l,max}$ value at a slightly higher angle of attack than the constant Mach number case. Differences were also observed in the magnitude and location of the peaks in C_l in the down-stroke phase. Similar differences were observed for C_d and C_m where the magnitude of the peak values were greater for the time-varying Mach number case. This suggests that the inclusion of unsteady freestream effects clearly affects dynamic stall data.

Gosselin et al. [16] has modelled one specific case of dynamic stall with unsteady freestream in CFD, in which shockwaves occur on the advancing side of the rotor. Gosselin also observed that the inclusion of unsteady freestream changed the aerodynamic behaviour of the airfoil. Similar to Kerho's observations, Gosselin et al. also observed non-linear variation in C_l in the up-stroke phase and higher peak values in all three aerodynamic coefficients.

Although the difference between the aerodynamic behaviour of constant freestream and variable freestream dynamic stall have been recognized and discussed in previous studies, whether this discrepancy compromises the accuracy of rotor analysis has not been investigated. There are other effects, such as radial flow and blade vortex interaction (BVI), which may cause significant differences from 2D steady freestream dynamic stall data and affect rotor analysis accuracy. However, this work aims to focus on quantifying the effect of time-varying freestream only.

2.2 Rotorcraft Comprehensive Analysis

Rotorcraft comprehensive analyses are computer codes that calculate the aeromechanical behaviour of the rotor such as blade motion and airloading, structural loads, vibration, and flight dynamics [30]. These codes are comprised of the most advanced models of structure, dynamics, and aerodynamics available in rotorcraft technology, and used in support of the parametric design and performance analysis of rotorcraft.

2.2.1 A Brief History of Rotorcraft Comprehensive Analysis

The development of rotor analysis codes started as soon as digital computers first became available in the 1960s [30]. In its initial developmental stage, the focus was on flight dynamics and structural loads, resulting in limitations in the range of analysis, i.e. the codes were often restricted to a specific rotor configuration. In the 1980s, a new generation of codes were developed addressing the limitations of the past codes. Through the use of modular and structured software architecture, the codes became much more flexible and versatile. Finite element models were developed around a similar time adding finite element and multibody dynamics modelling capabilities. The input-driven definition of the geometry commonly seen in the current rotor analysis codes were introduced shortly after. Utilizing the advances in high-performance computing technologies in the late 1990s and early 2000s, significant efforts were made to improve the rotor aerodynamics

via CFD. Methods of coupling the rotor analysis codes with CFD were developed to manage structural dynamic response, aircraft trim, and wake modelling [30].

2.2.2 Dynamic Stall Handling in Rotorcraft Comprehensive Analyses

In current rotorcraft comprehensive analyses such as CAMRAD II, semi-empirical dynamic stall models are used to generate the unsteady aerodynamic coefficients of the blade sections undergoing dynamic stall [31]. They require much less computational resources than other methods such as unsteady Reynolds-averaged Navier-Stokes (URANS) CFD, making them attractive for rotor analysis applications. Semi-empirical dynamic stall models require several coefficients that are empirically calculated based on experimental unsteady airfoil data. However, the experimental data from which the coefficients are deduced are of a limited number of airfoils at a limited range of Mach numbers. Thus, their accuracy lacks consistency across various flight regimes, especially in high Mach number conditions. Some of the most widely used semi-empirical dynamic stall models are described in the following section.

2.2.2.1 Semi-Empirical Dynamic Stall Models

Although the mathematical formulations differ amongst various semi-empirical dynamic stall models, they share a similar underlying physics. The two widely used dynamic stall models, Leishman-Beddoes (L-B) model and ONERA EDLIN model, use a delayed stall with lift and moment increments calculated from the leading-edge vortex. The L-B model computes the non-linear lift, drag, and pitching moment directly from the static airfoil look-up tables. Once the vortex shedding is initiated, the LEV is modelled by a first-order linear dynamic model. This model requires eight parameters [32]. The ONERA EDLIN model uses three second-order differential equations to calculate the leading vortex load increments, driven by the differences between the linearity and non-linearity of lift, drag, and pitching moment requiring 22 parameters [31]. A

detailed explanation of the mathematical formulation of these models can be found in Ref. [33] for the L-B model, and Ref. [34] for the ONERA EDLIN model.

The accuracy of the L-B and ONERA EDLIN models are illustrated in Figure 2.3 and Figure 2.4 by comparing the results generated with the dynamic stall models to experimental data.

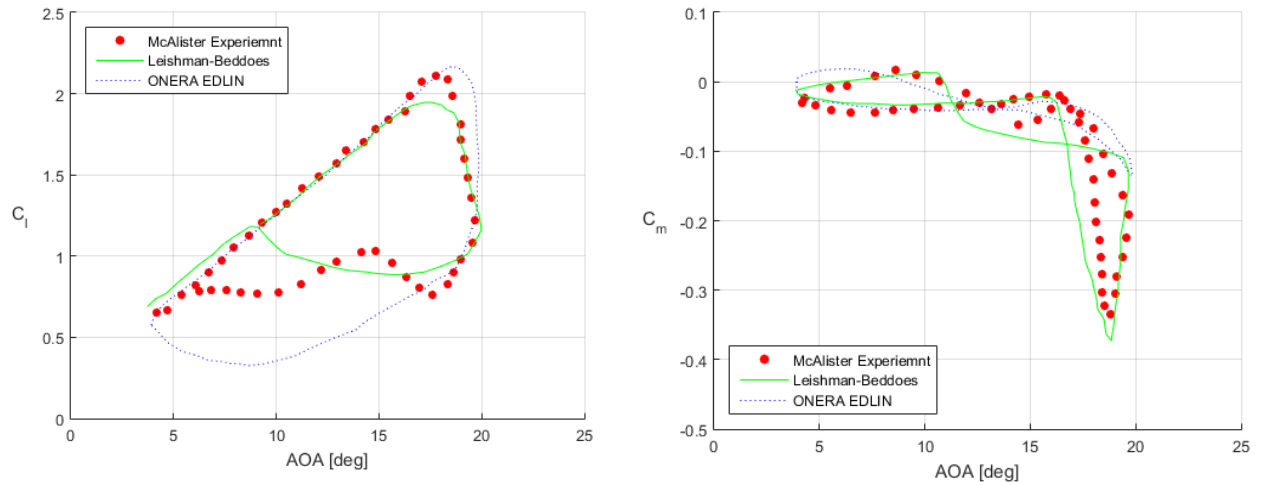


Figure 2.3: Comparison of experimental dynamic stall data to results computed with L-B and ONERA EDLIN model on SC1095 airfoil at $M = 0.301$, $Re = 3.98 \times 10^6$, $\alpha = 11.86^\circ \pm 7.9^\circ$, experimental data from Ref. [11].

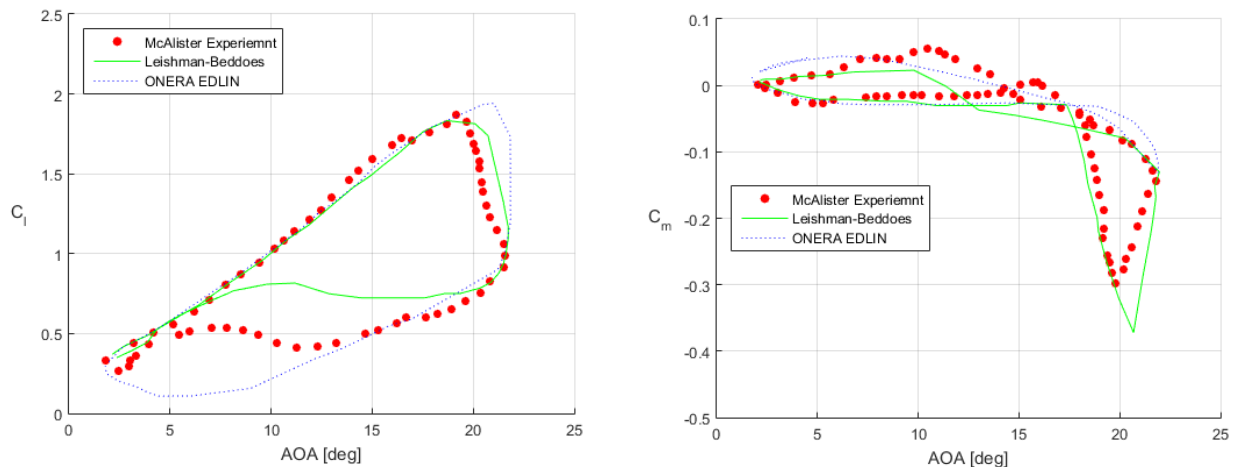


Figure 2.4: Comparison of experimental dynamic stall data to results computed with L-B and ONERA EDLIN model on NACA0012 airfoil at $M = 0.301$, $Re = 3.98 \times 10^6$, $\alpha = 11.86^\circ \pm 7.9^\circ$, experimental data from Ref. [11].

Figures 2.3 and 2.4 show the data for the SC1095 airfoil and NACA0012 airfoil, respectively for the same flow conditions. The agreement between the dynamic stall model data and the experimental data is respectable for both cases, however deficiencies can certainly be seen. Both models show good accuracy in the up-stroke phase (AOA is increasing), but the semi-empirical data does not match well with the experimental data in down-stroke phase or with one another. This highlights dynamic stall models' weakness in capturing the hysteresis effect and different levels of accuracy demonstrated by different models. It also appears that the accuracy of the dynamic stall models depends on the geometry of the airfoil, and it is likely that it is also dependent on the flow conditions. Moreover, as discussed previously these dynamic stall models generate the aerodynamic data at a constant Mach number when different aerodynamic behaviour is exhibited under unsteady Mach number conditions.

2.3 UH-60A Airloads Program

The UH-60A Airloads Program was a joint project headed by NASA and the U.S. Army from 1993 to 1994. Instrumented rotor blades were designed and manufactured for the UH-60A helicopter to be installed on a UH-60A at NASA Ames Research Center. The rotor blades were equipped with 241 pressure transducers on one blade, and a set of strain gauges and accelerometers on a second blade. A special purpose data acquisition system was developed for this program to acquire rotating system measurements [35].

One of the main objectives of this program was to acquire comprehensive and accurate airloads data over the complete operating limits of the UH-60A helicopter. In 31 flights, over 900 different test conditions were recorded and processed. Some processed data are available in the open literature, and it has been serving as an excellent source for validating rotor analysis codes.

2.3.1 Counter 9017 Case from UH-60A Airloads Program

Flight test data for a steady-level flight case with a designation Counter 9017 is well documented in literature. In addition to the flight test blade airloads data, blade airloads calculated by CAMRAD II with various semi-empirical dynamic stall models are also available for this test case, providing excellent comparison data. Moreover, a dynamic stall rotor map produced by Bousman [6] is available for this case. Table 2.2 summarizes the conditions of Counter 9017, and Figure 2.5 shows the dynamic stall rotor map plotted by Bousman.

Table 2.2: Counter 9017 description.

Counter	C_T/σ	μ	M_∞	M_{tip}
c9017	0.129	0.24	0.157	0.665

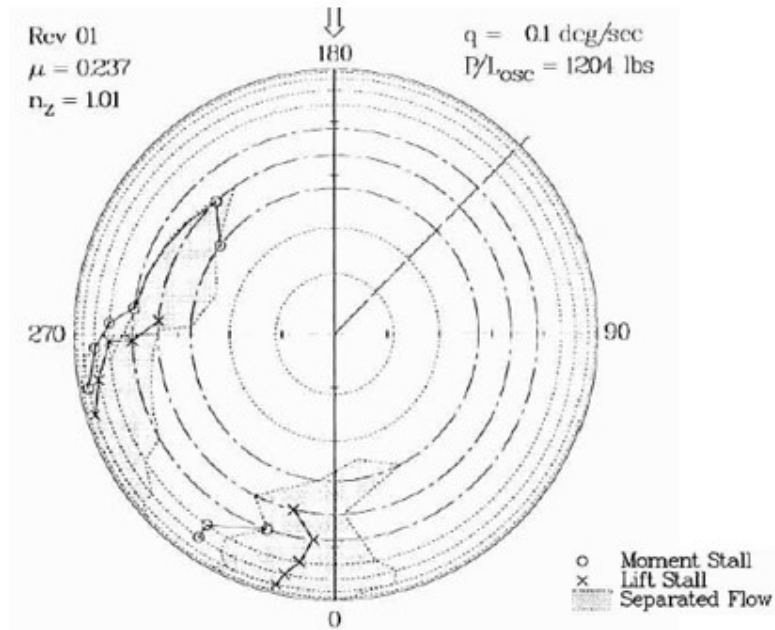


Figure 2.5: Dynamic stall rotor map for Counter 9017 [6].

As seen in Figure 2.5, much of the outboard region of the blade is under dynamic stall, stall being triggered near the 270 degree azimuth position where the AOA reaches its maximum value. The information given by the dynamic stall rotor map can be used to defined the stalled region in the rotor analysis code to reduce uncertainty.

The data reduction process and the error estimation of the flight test data from the UH-60A Airloads Program are not described in detail in the open literature. Therefore, the flight test data is better suited for qualitative analyses where the general capturing of the important characteristics such as the stall events are examined.

2.3.2 Semi-empirical Dynamic Stall Model Validation

In 1998, Nguyen and Johnson [32] evaluated five dynamic stall models with rotorcraft comprehensive analysis code CAMRAD II. The five models evaluated were the Johnson, Boeing, Leishman-Beddoes, ONERA EDLIN, and ONERA BH models. The evaluation study considered the flight test conditions of Counter 9017 discussed in Section 2.3.1. Figure 2.6 shows the comparison of the CAMRAD II results to the flight test data. The results generated with the Leishman-Beddoes and ONERA BH models are not shown in Figure 2.6 since Leishman-Beddoes model results were virtually identical to the quasi-steady aerodynamics model, and the results with the ONERA BH model were divergent.

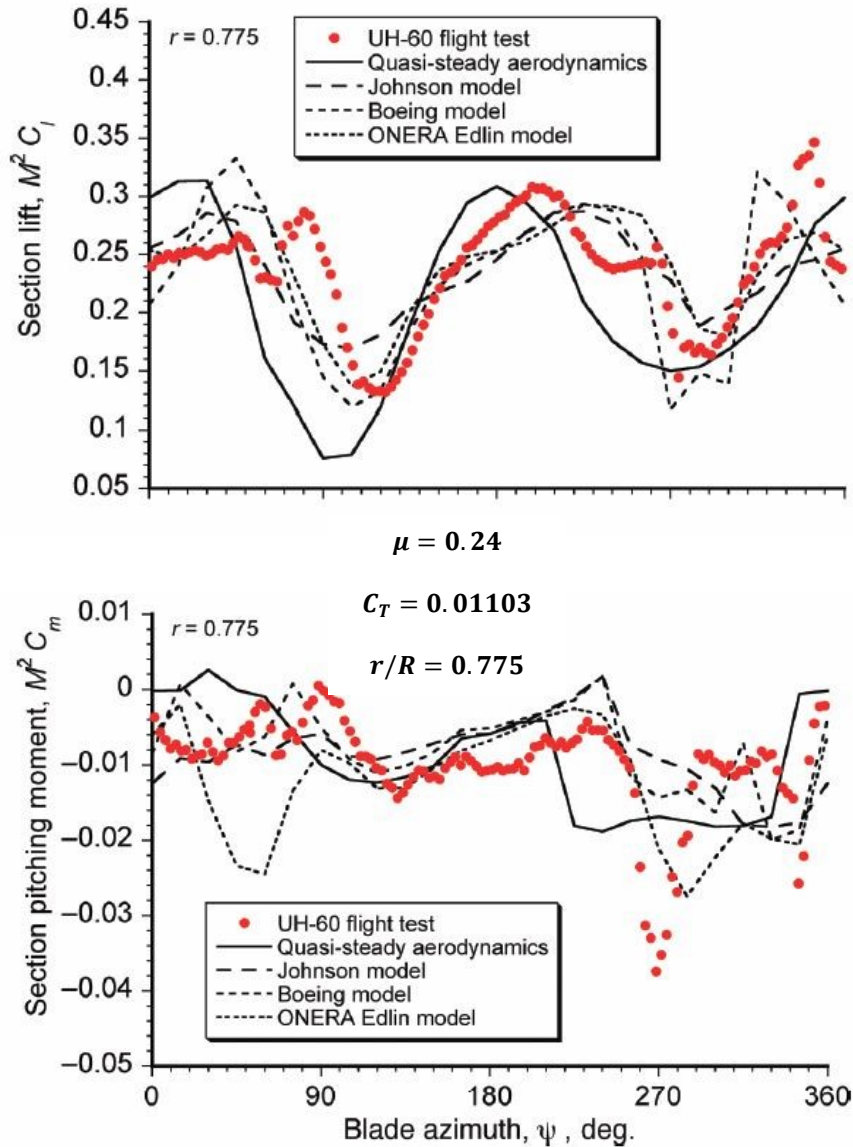


Figure 2.6: Comparison of flight test data with computed results using dynamic stall models (adapted from Ref. [8]).

For the section lift history, the accuracy of the CAMRAD II results are fair in capturing the general trend. However, all models fail to match the magnitude and capture the stall events accurately. They also show a significant discrepancy among themselves. A similar level of accuracy is shown in the section pitching moment history. While the general trend is captured by some models, all failed to predict the two stall events between 270 and 360-degree blade azimuth position. The discrepancy among the models is more prominent in the pitching moment results.

The discrepancy between the flight test data and the numerical results leads to the question of whether the error is caused by the use of semi-empirical dynamic stall models for the generation of dynamic stall aerodynamic data. Although BEMT based rotor analysis codes such as CAMRAD II has limitations in modelling 3D effects such as span-wise flow and tip loss, using CFD generated unsteady dynamic stall data for forward flight analysis can quantify the effect of semi-empirical dynamic stall models on the accuracy of the rotor analysis results.

Chapter 3

Numerical Methods

Two computational tools were used for the aerodynamic analysis of the rotor: *Qoptr*, an in-house Blade Element Momentum Theory (BEMT) based rotor analysis code, and ANSYS Fluent, CFD software which was used to generate the 2D aerodynamic data of the blades sections of the UH-60A helicopter. The following sections describe these two computational codes in detail, and the coupling of these two codes, i.e. implementing dynamic stall aerodynamic data in *Qoptr*.

3.1 *Qoptr* (Rotor analysis code)

Qoptr is an in-house code developed by Carleton University's Rotorcraft Research Group in 2014. It is a Blade Element Theory-based rotor analysis code that calculates the aeromechanical behavior of helicopters including performance, trim, blade motion, and airloading. The *Qoptr* framework is capable of handling fully articulated rotor hubs as well as teetering rotor hubs, and is comprised of two simulation modules: the hover module and forward flight module. Both modules have been validated with appropriate experimental data available in the literature. A detailed explanation of the validation can be found in Ref. [36].

The hover module is used to analyze rotors in hover or axial climb. This module assumes axisymmetric flow conditions and uses a BEMT approach to determine the induced inflow distribution. The forward flight module, on the other hand, utilizes prescribed inflow models to define the induced inflow distribution at the rotor disk to simulate non-zero advance ratio conditions (i.e. non-zero forward flight speed). Both modules use the lifting-line theory based

aerodynamics model, and use pre-generated airfoil data that is organized into look up tables as a function of Reynolds number and angle of attack. The code also features a blade dynamics model, which allows to prescribe the feathering and predict the flapping and lead-lag motions of the blade. The blade dynamics model assumes rigid blades. A detailed description of the aerodynamic analysis is omitted in this thesis, as it is not the main focus. Moreover, the theory and mathematical background of modern rotor analysis tools are already well established in the literature and in many rotorcraft textbooks.

3.1.1 Blade and Azimuth Discretization Dependence Study

In blade element theory (BET) based rotor analysis codes, the blade is discretized into two-dimensional sections in the span-wise direction, and the loading is calculated at each section. In forward flight analysis, where the flow is no longer axisymmetric, the discretization of the rotor must be extended in the azimuthal direction. Thus, similar to grid dependence studies done in grid based CFD, a blade and azimuth discretization dependence study should be done prior to analysis. Span-wise blade discretization for hover analysis of UH-60A rotor was first carried out. It was found that at 100 elements ($N=100$), the figure of merit, power coefficient, and collective angle showed convergence. For hover analysis, computation time increase with increasing number of elements was not an issue as all calculations were computed in less than 20 seconds.

For forward flight analysis, a discretization dependence study was extended in the azimuthal direction. The flight conditions of the c9017 shown in Table 2.2 were used.

Table 3.1: Discretization dependence study for forward flight analysis for Counter 9017 at $C_T/\sigma = 0.129$, $\mu = 0.24$.

	N=50	N=100	N=150	N=200	N=250
C_p	0.000656	0.000644	0.000609	0.000886	0.000886
Collective [°]	8.66	8.63	9.19	11.26	11.26
Time [s]	45.29	50.58	56.7	263	366

As seen in Table 3.1, for 200 blade elements in the span-wise direction were required to achieve solution convergence. In the azimuthal direction, it was found that 90 elements were necessary. Therefore, it was determined that 100 span-wise blade elements are required for hover analysis, and 200 span-wise blade elements and 90 azimuthal elements are required for forward flight analysis.

3.1.2 Input Parameters to *Qopt*

Major inputs to *Qopt* include physical rotor parameters, blade geometry, and flight conditions. The physical rotor parameters and the blade and airfoil geometry of the UH-60A rotor were obtained from literature [37] and the flight conditions were obtained from the UH-60A Airload Program [35]. Figures 3.1 and 3.2 illustrate the blade and airfoil geometry, respectively. Table 3.2 summarizes key numerical parameters used in *Qopt* for the UH-60A helicopter.

For the trim conditions of the rotor, the test data for the Counter 9017 were used. The lateral and longitudinal cyclic angles were set at 9 and -7 degrees, respectively, and the tilt angle was set 3 degrees.

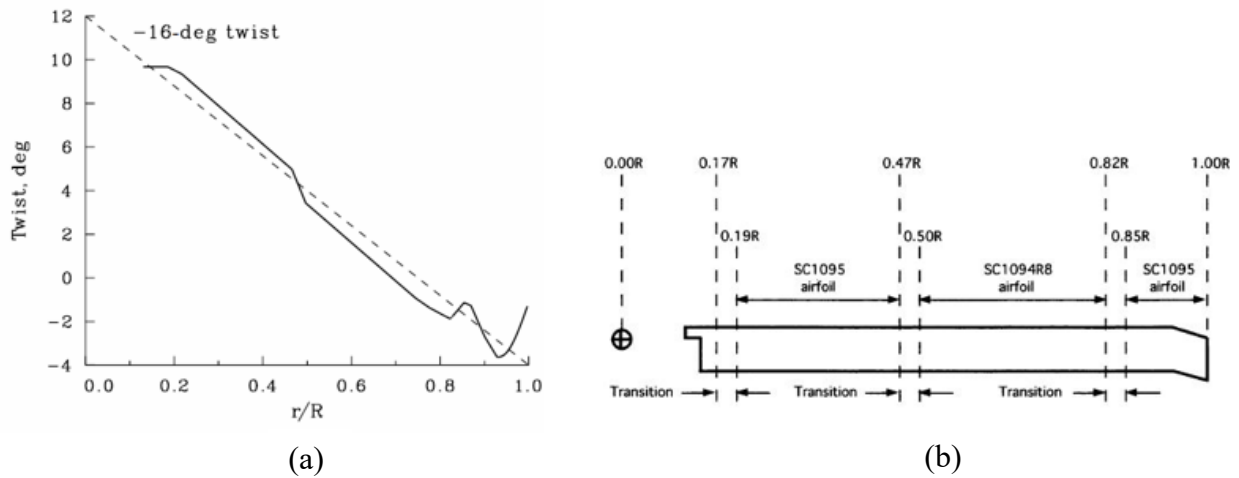


Figure 3.1: UH-60A blade geometry (a) blade twist and (b) airfoil distribution [45].



Figure 3.2: Airfoils on UH-60A rotor blade (a) SC1095 and (b) SC1094 R8 [45].

Table 3.2: Rotor parameters used in Qoptr for UH-60A.

Number of blades	4
Rotor diameter [m]	16.368
Rotor RPM [-]	258
Root cut-out [% rotor radius]	16
Solidity [-]	0.0826
Flapping hinge location [% rotor radius]	4.66
Lead-lag hinge location [% rotor radius]	4.66
Blade mass [kg] *	116.75

Flapping spring stiffness [Nm/deg] *	0
Lead-lag damper constant [Nm/(deg/s)] *	100

* Estimated value

To validate the integrity of the obtained rotor parameters and the blade geometry in the *Qoptr* environment, hover flight was analyzed at various thrust settings with *Qoptr*, and its results were compared to the flight test data from the UH-60A Airload program. Since dynamic stall does not occur in hover flight, only the quasi-steady CFD aerodynamic data of SC1095 and SC1094 R8 was used in the analysis which had been validated with experimental data available in Ref. [38]. Two important performance parameters in hover flight, figure of merit, and power coefficient were considered. The comparison of the numerical results to the flight showed good agreement between the two sets of data as shown in Figure 3.2, indicating good representation of the rotor parameters and the blade geometry in *Qoptr*.

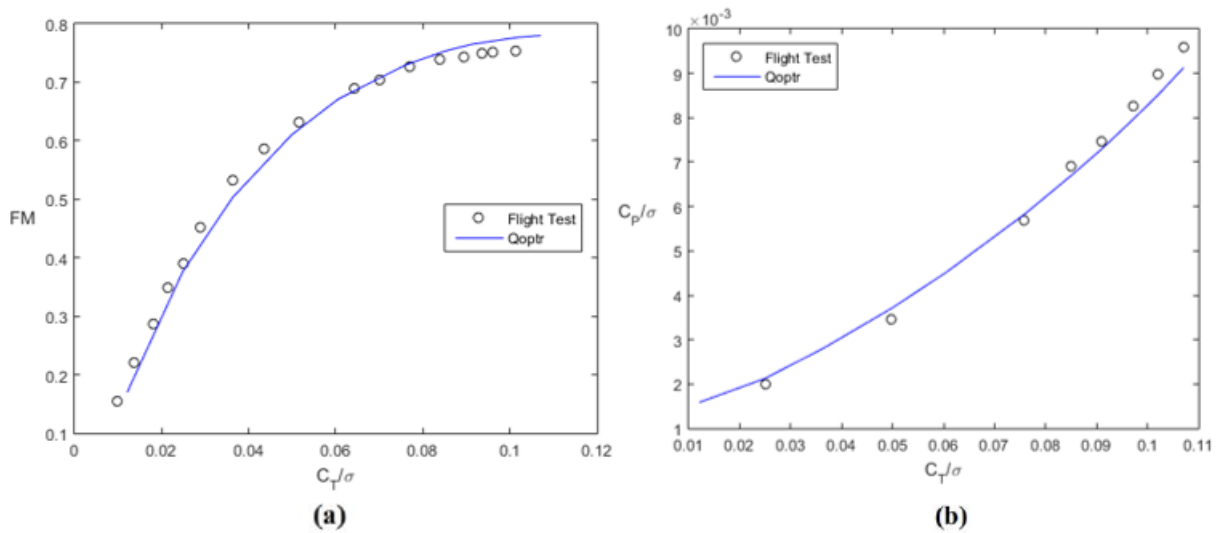


Figure 3.3: Validation of Qoptr hover results (a) figure of merit and (b) power coefficient.

3.2 Computational Fluid Dynamics (CFD)

The blades on the UH-60A helicopter are comprised of two airfoils, SC1095 and SC1094 R8, as seen in Figure 3.1 (b). The two airfoils were modelled in a 2D environment and their aerodynamic coefficients were obtained with ANSYS Fluent CFD code. The aerodynamic coefficients were obtained at quasi-steady, constant freestream dynamic stall, and unsteady freestream dynamic stall conditions. The development, verification, and validation processes for the three conditions are discussed in the following sections.

3.2.1 Quasi-steady Case

Since the quasi-steady case was the simplest in complexity, the CFD methodology development started with the quasi-steady case. In quasi-steady conditions, the rate of angle of attack variation is zero or low, i.e. the reduced frequency is less than 0.05. Quasi-steady aerodynamic data is required for analyzing hover flight in which the blade sections maintain a constant angle of attack throughout the azimuth. It is also used in forward flight analysis since not the entirety of the blade is under dynamic stall.

3.2.1.1 Computational Domain and Boundary Conditions

The far-field distance of the computational domain was determined following Blazek's [39] recommendation where he suggests that a far-field distance of at least $100c$ is required to negate the need for vortex correction in the solver for high Mach number cases. Figure 3.4 illustrates his recommendation.

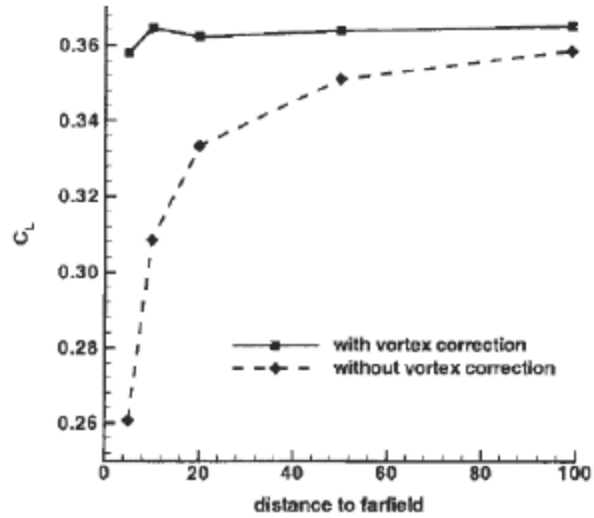


Figure 3.4: Effect of far-filed distance on lift coefficient of NACA 0012 at $M = 0.8$ and $\alpha = 1.25^\circ$ [15].

Since high Mach number conditions occur on the outboard region of the blades, and implementing the vortex correction to the Fluent code was found to be not trivial, a far-field distance of $250c$ was chosen. The domain was rectangular in shape as shown in Figure 3.5.

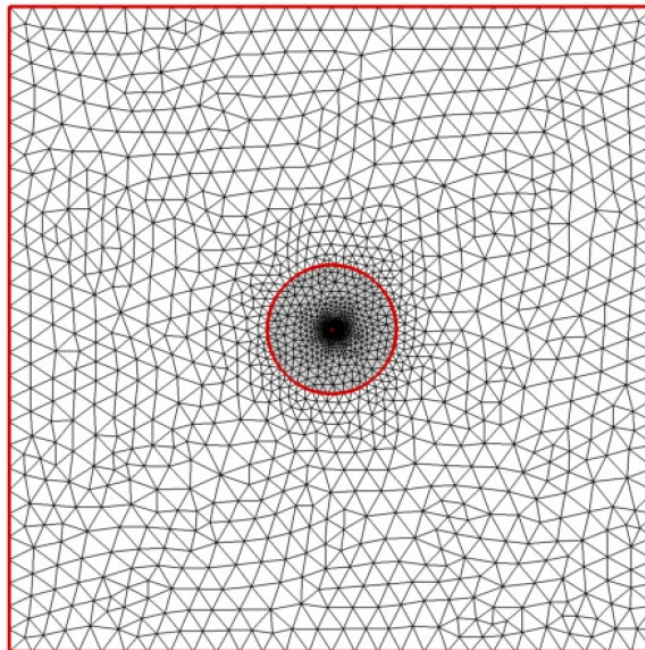
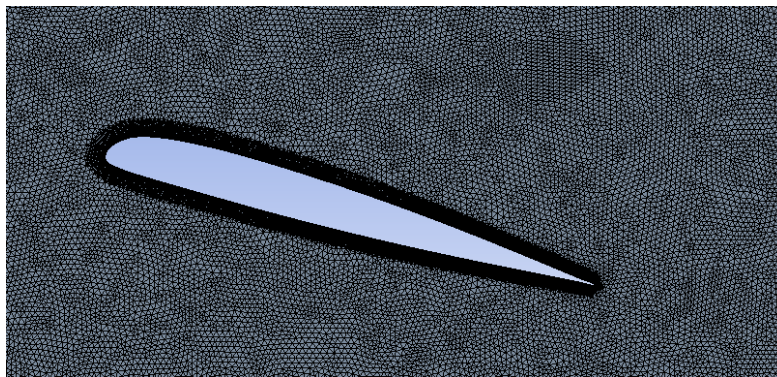
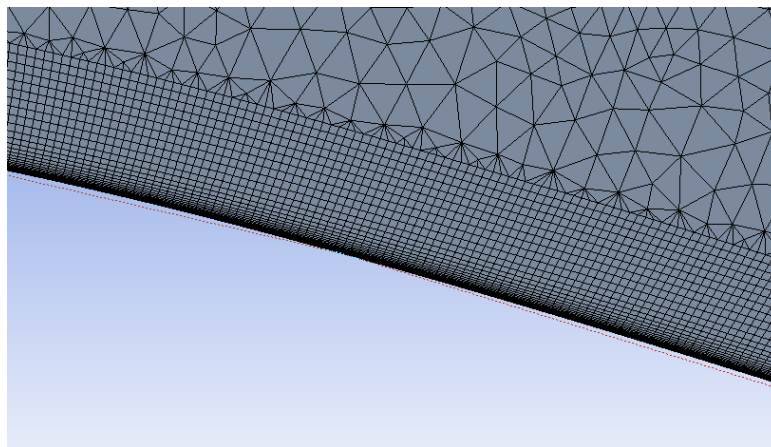


Figure 3.5: Full view of computational domain.

Due to its similarity in shape to the airfoils used on the blades of UH-60A and its expansive validation data, the NACA 0012 airfoil was used in the initial grid validation tests. The grid dependence test led to a grid with 192,676 elements as seen in Ref. [13]. Except for the boundary layer region around the airfoil, unstructured triangular cells were used. For the boundary layer region, structured rectangular cells were used to generate 40 inflation layers, keeping the y^+ value near one. To capture the shockwave on the upper surface of the airfoil and the vortices in the downstream region, the mesh near the airfoil was refined. The details of the grid can be in Figure 3.6.



(a)



(b)

Figure 3.6: Computational domain (a) refined region around airfoil and (b) inflation layers in boundary layer.

The left boundary of the computational domain was set as velocity inlet and the right boundary was set as pressure outlet. The top and bottom boundaries were set as free-slip wall. The airfoil surfaces were set as no-slip wall. The Spalart-Allmaras turbulence model was used with 1% intensity. Table 3.3 summarizes the main numerical parameters of the setup.

Table 3.3: Main simulation parameters.

Parameter	Value
Domain size	250c
Grid size	192,676 cells
Turbulence model	Spalart-Allmaras ($I = 1\%$)
Wall y^+	≤ 1

3.2.1.2 Shockwave Capturing

To verify that the grid captures the shockwave that appears in high Mach number flow conditions, a high Mach number flow was simulated on the SC1095 airfoil at $M = 0.7$. As seen in Figure 3.7, the expected shockwave was captured well by the grid illustrated by a sudden drop in the Mach number.

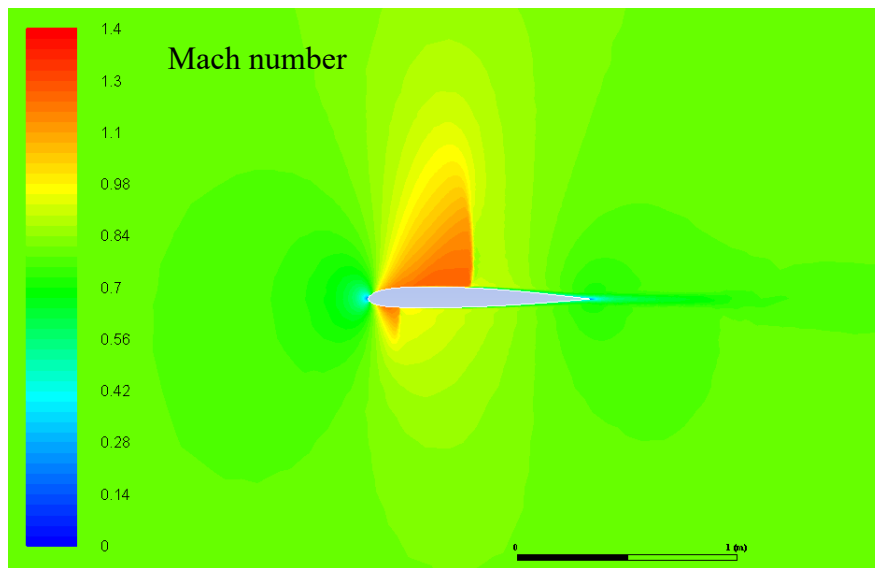


Figure 3.7: Verification of high Mach number flow condition.

3.2.1.3 CFD Validation

Validation of the CFD method was done at both low and high Mach number conditions by comparing the CFD results to experimental data. For the high Mach number condition the NACA 0012 airfoil was considered, and for the low Mach number case the SC1095 airfoil was considered. For both cases, there was excellent agreement between the CFD data and the experimental data, indicating a high level of accuracy of the CFD setup in low and high Mach number conditions. The comparison of the CFD and experimental data are shown in Figures 3.8 and 3.9.

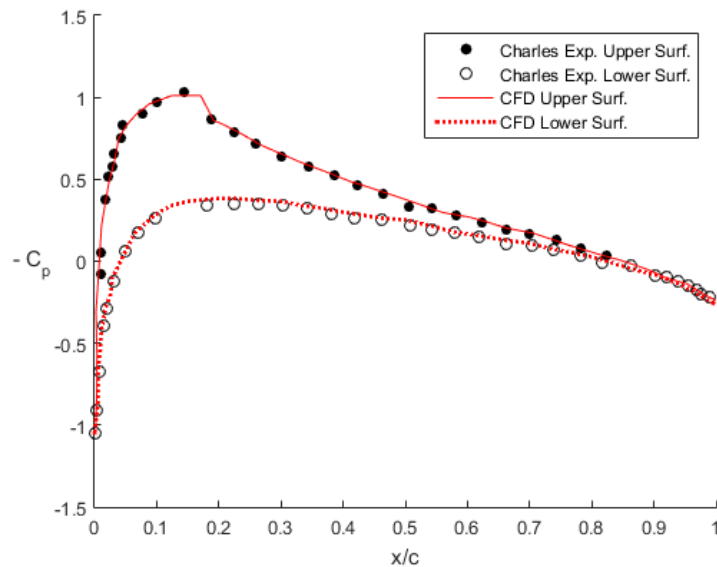


Figure 3.8: High Mach number case validation with NACA0012 at $M = 0.7$, $Re = 9 \times 10^6$, and $\alpha = 1.49^\circ$ (Experimental data from Ref. [40]).

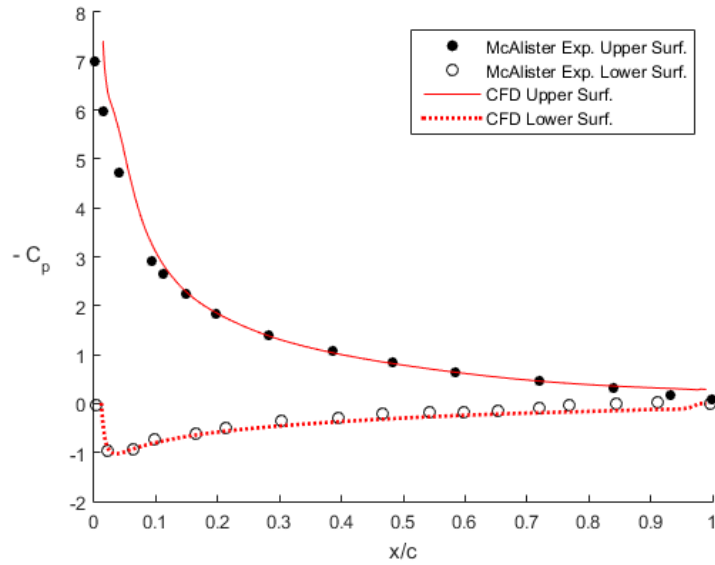


Figure 3.9: Low Mach number case validation with SC1095 at $M = 0.3$, $Re = 3.88 \times 10^6$, and $\alpha = 13.5^\circ$ (Experimental data from Ref. [11]).

3.2.2 Constant Freestream Dynamic Stall Case

In the constant freestream dynamic stall case, the airfoil is undergoing oscillating pitching motion of a given amplitude and frequency while the freestream Mach number is held constant. This requires utilization of a dynamic mesh adding complexity to the simulation. The following sections describe the development of the dynamic mesh, and the verification and validation of the simulation.

3.2.2.1 Computational Domain and Boundary Conditions

The computational domain and the main boundary conditions for the constant freestream dynamic stall case stayed unchanged from the quasi-steady case. A separate grid dependence study for the constant freestream dynamic stall case showed grid independence at the same grid density as the quasi-steady case. The details of the grid dependence test can be found in section 3.2.2.3. Table 3.4 summarizes other key parameters used in the simulation.

Table 3.4: Summary of simulation parameters for constant freestream case.

Numerical Parameter	Value
Size of computational domain	250c
Mesh size	192,676
Time resolution	3,000 time-steps/cycle
Initial conditions	Steady state solution at mean AOA
Turbulence model	Spalart-Allmaras ($I = 1\%$)

Since a dynamic stall simulation requires the airfoil to pitch up and down during the simulation, a moving mesh technique had to be implemented. A moving mesh can be achieved using a dynamic mesh or a sliding mesh in CFD. In the CFD simulation presented in this work, the sliding mesh technique was employed as it involves no mesh deformation. This technique ensures that the intended grid density and structure in the boundary layer and in the wake region where the vortex shedding takes place are kept constant.

To implement the sliding mesh technique for the pitching of the airfoil, a separate circular domain was created around the airfoil, establishing an interface with the main domain as seen in Figure 3.10.

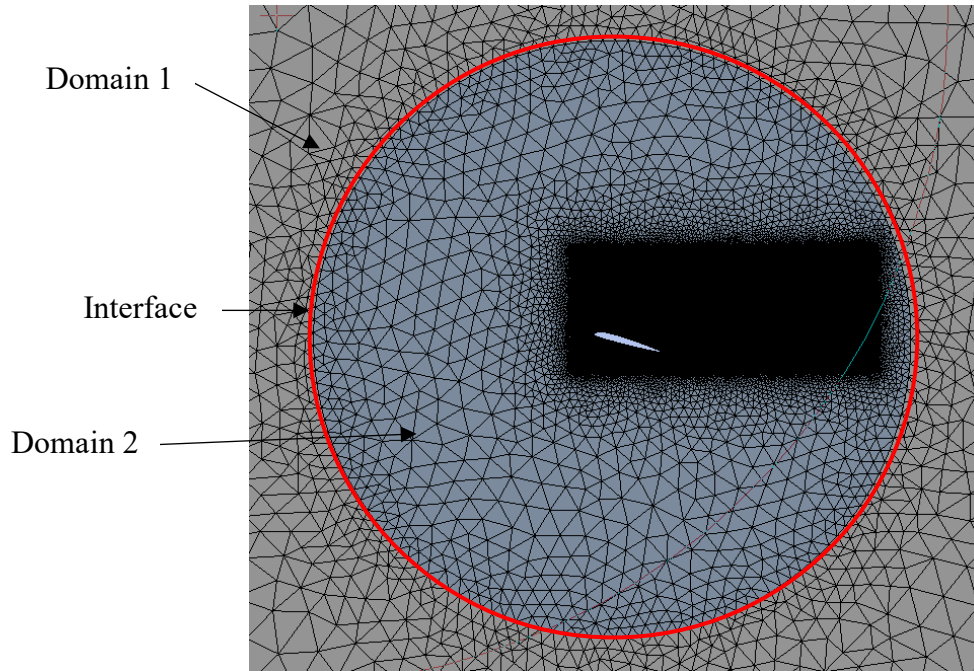


Figure 3.10: Circular domain around the airfoil.

The circular domain, coloured in blue, rotates relative to the grey main domain, thereby pitching the airfoil and changing the angle of attack.

3.2.2.2 Initial Conditions

The constant freestream dynamic stall simulation is structured in two parts. The first part is a steady-state simulation with the airfoil at the mean angle of attack. The converged solution of this simulation is used as the initial conditions for the second part, which is a transient simulation. It is in the second part where angle of attack is varied and dynamic stall aerodynamic data is obtained. Using the steady-state solutions as the initial conditions rather than initializing the entire domain with the freestream Mach number improves convergence characteristics.

3.2.2.3 Angle of Attack Oscillation

The pitching motion of the airfoil was defined using a sinusoidal function. Although the angle of attack oscillation is not perfectly sinusoidal in real flight, a sinusoidal function can be used to closely resemble the variation of the blade angle of attack by using appropriate amplitude and frequency. Whereas the frequency of the motion is dictated by the rotor frequency of the helicopter in question, multiple amplitudes need to be considered since its true value is not known from the flight tests. The amplitude of the pitching motion of the airfoil is rather determined by the rotor analysis code for a given thrust coefficient in an iterative manner. Figure 3.11 shows a sample angle of attack variation as a function of blade azimuth.

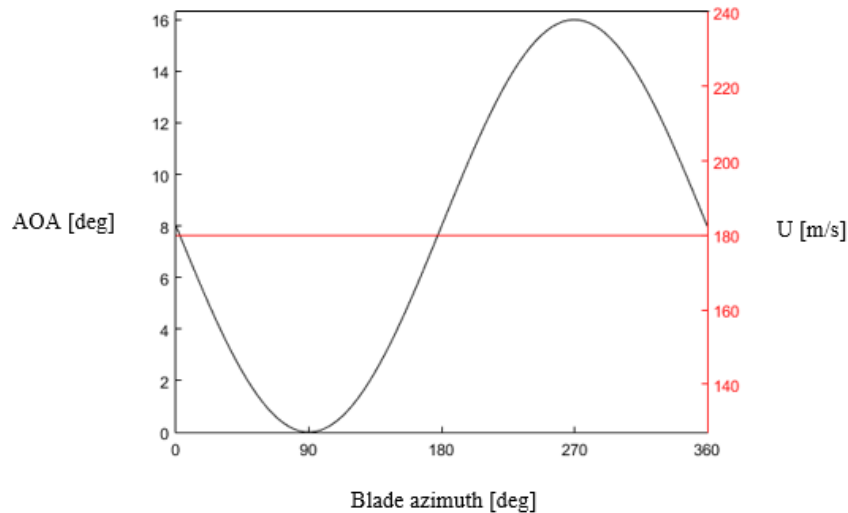


Figure 3.11: A sample angle of attack variation as a function of blade azimuth for constant freestream case.

3.2.2.4 Cycle Periodicity Convergence

In addition to solver residual convergence, the periodicity of the aerodynamic results was also verified. In their studies, Kerho [27] and Gharali et al. [29] observed periodicity within 2.5 pitching

cycles. The initial simulation was run for 5 pitching cycles at a Mach number of 0.5 for the SC1094 R8 airfoil, and periodicity was achieved after two cycles as shown in Figure 3.12.

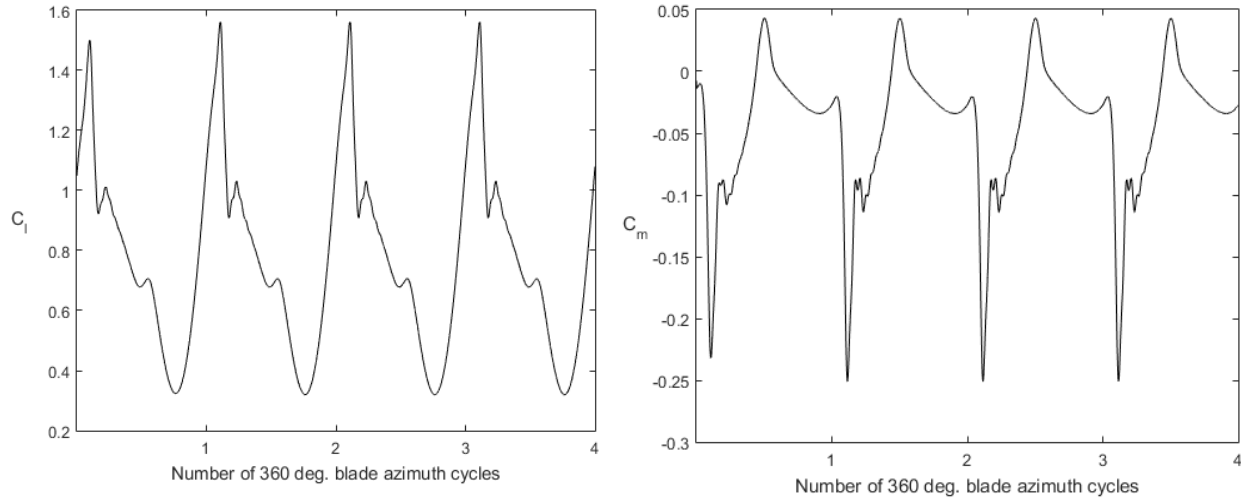


Figure 3.12: Time history of aerodynamic loads.

3.2.2.5 Verification and Validation

For verification and validation of the constant freestream dynamic stall case, a case from Ref. [11] was considered due to its availability of experimental data and relevant flow conditions. Table 3.5 summarizes the test conditions of the selected case.

Table 3.5: Validation case test conditions.

Airfoil	Mach number	Reynolds number	AOA [deg]	Reduced Frequency
SC1095	0.301	3.98×10^6	11.88 ± 7.90	0.100

A grid dependence study was performed using three levels of refinement, where the medium grid had the same level of refinement as the grid used in the steady case. It was found that grid independence was achieved with the medium grid as seen in Figure 3.13. The coarse, medium and fine grids had 99,300, 192,676, and 260,918 elements, respectively. For the temporal domain, 2000

time-steps per pitching cycle with 100 inner iterations were used as previously used in other CFD dynamic stall studies [14], [13].

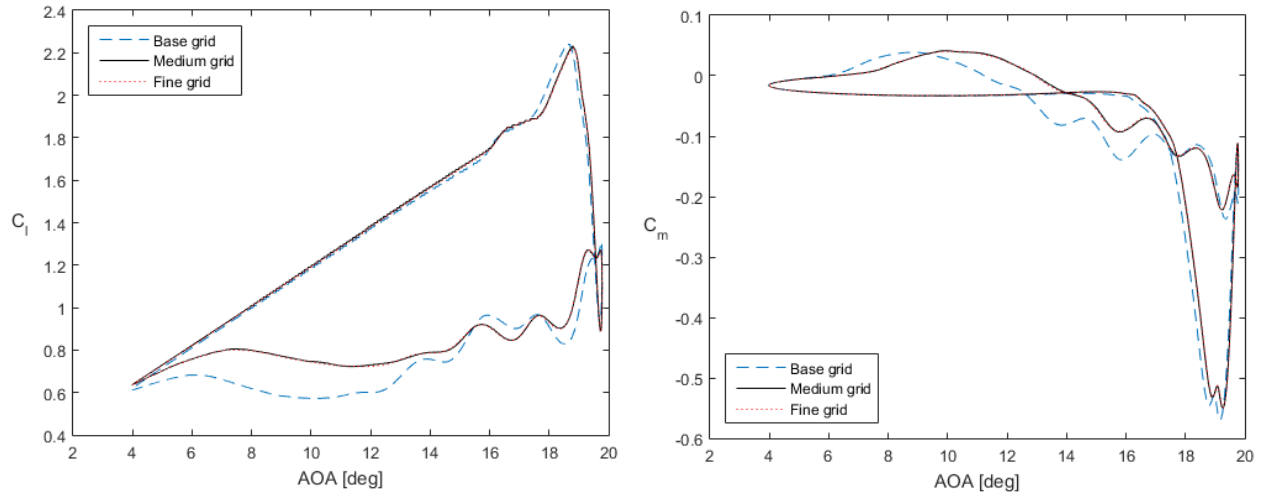


Figure 3.13: Grid dependence test for constant freestream case.

The grid converged results were then compared to the experimental data obtained from Ref. [11]. As shown in Figure 3.14, respectable agreement was observed between the CFD data and the experimental data.

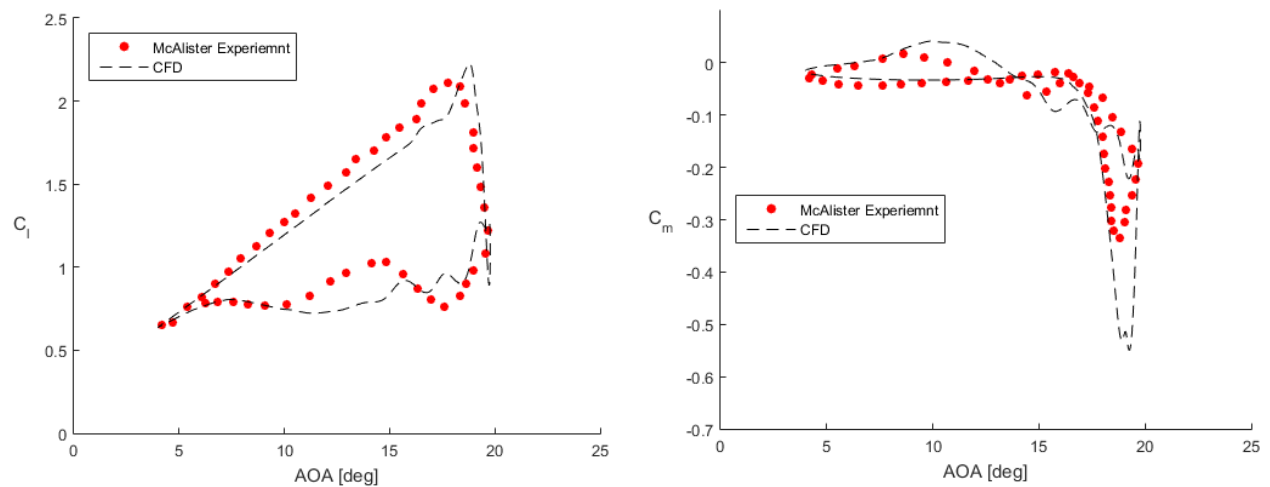


Figure 3.14: Comparison of CFD data to experimental data for constant freestream dynamic stall case.

Similar to other CFD dynamic stall studies, the moment peak was overpredicted by CFD. Both Richter et al. [12] and Al-Jaburi [13] observed a similar level of overprediction as discussed in

Section 2.1.1. Since the magnitude of the moment peak is known to be sensitive to the turbulence model, the simulation was run with the SST turbulence model as well. The simulation run with the SST turbulence model overpredicted the moment peak by a larger margin and showed lower accuracy overall.

3.2.3 Time-varying Freestream Dynamic Stall Case

The time-varying or unsteady freestream dynamic stall case is identical to the constant freestream case discussed in the previous section except for the inlet boundary condition. In the unsteady freestream case, an unsteady boundary condition is imposed to the inlet where the inlet velocity is calculated at each time-step with an prescribed equation in a user defined function (UDF). The sinusoidal motion of the velocity is 180 degrees out of phase.

3.2.3.1 Fluctuating Velocity Inlet Condition

Similar to the oscillating motion of the airfoil, the unsteady freestream velocity was modelled with a sinusoidal equation. Unlike the equation of motion of the airfoil, both the frequency and the amplitude are known for the fluctuating velocity because the advance ratio and the radial location dictate the velocity seen by a blade section. Figure 3.15 shows a sample case of oscillating airfoil and inlet velocity against the blade azimuth.

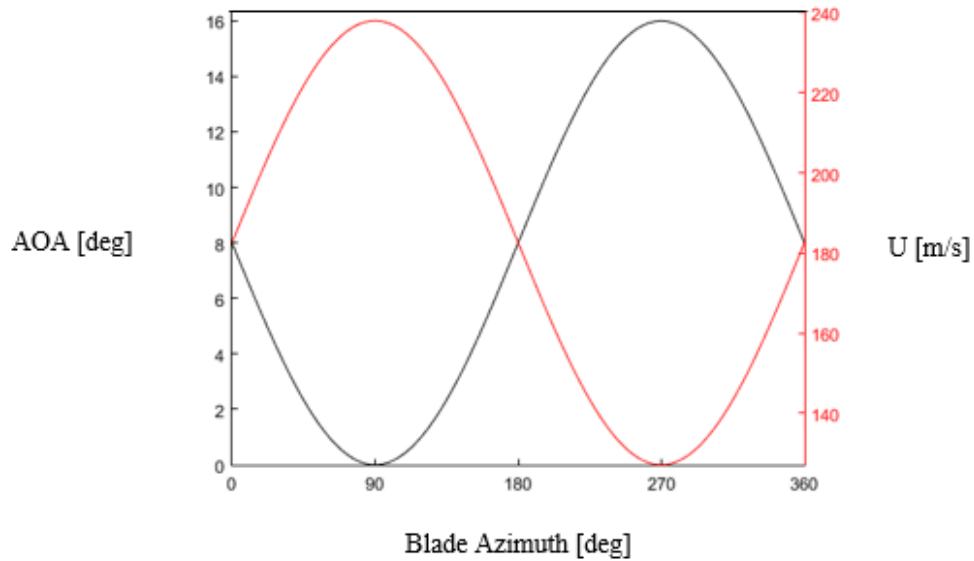


Figure 3.15: A sample angle of attack and inlet velocity variation as a function of blade azimuth for unsteady freestream case.

3.2.3.2 Verification

Since the inlet boundary condition has changed, another series of grid and time-step dependence tests were performed. Similar to the constant freestream case, three levels of grid density were used. The coarse, medium and fine grids had 99,300, 192,676, and 260,918 elements, respectively. Identical to the constant freestream case, grid independence was achieved with the medium grid and time-step independence was achieved at 2000 time-steps per pitching cycle and 100 inner iterations as seen in Figure 3.16.

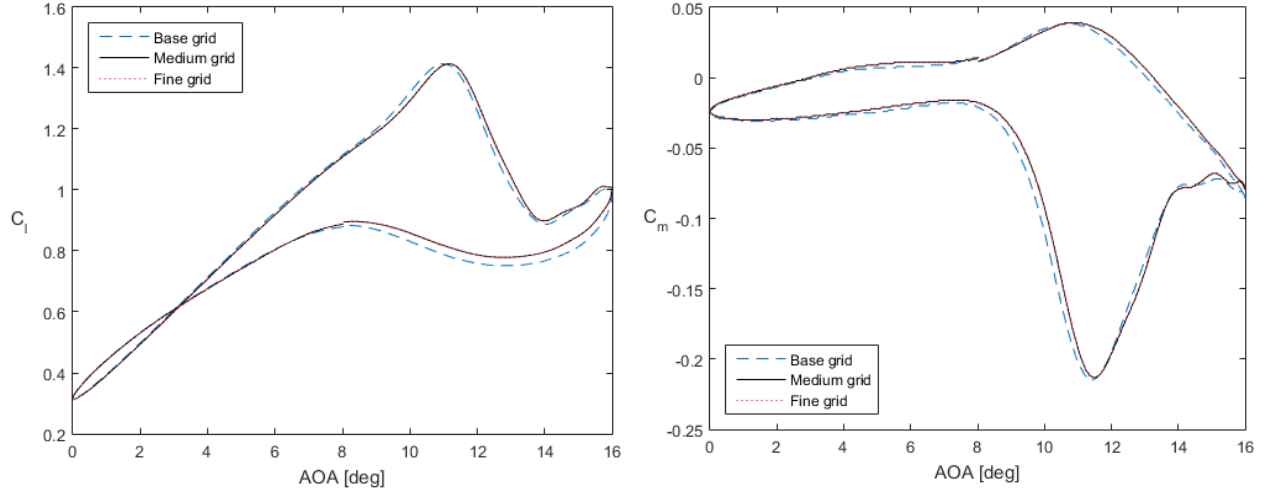


Figure 3.16: Grid dependence study for unsteady freestream dynamic stall case at $M = 0.53 \pm 0.16$ and $\alpha = 8^\circ \pm 8^\circ$.

3.2.3.3 Application of Time Lag

Since the inlet velocity is applied at the inlet boundary which is 250 chord lengths away from the airfoil, a change in velocity at the inlet will only affect the airfoil at the airfoil once it has convected downstream to the airfoil. Poinso and Lele [41] defined the propagation velocity of a wave travelling with the airflow as the sum of the wave speed and the speed of sound in the medium. Therefore, the time lag can be calculated as seen in Equation 3.1.

$$t_{lag} = \frac{250c}{a + U_{inlet,mean}} \quad (3.1)$$

This time lag was tested in the ANSYS Fluent code by observing the velocity history at the inlet boundary and at the quarter chord location of the airfoil at flow conditions representative of $r/R = 0.775$. The observed time lag was in agreement with the value calculated with Equation 3.1 as seen in Figure 3.17.

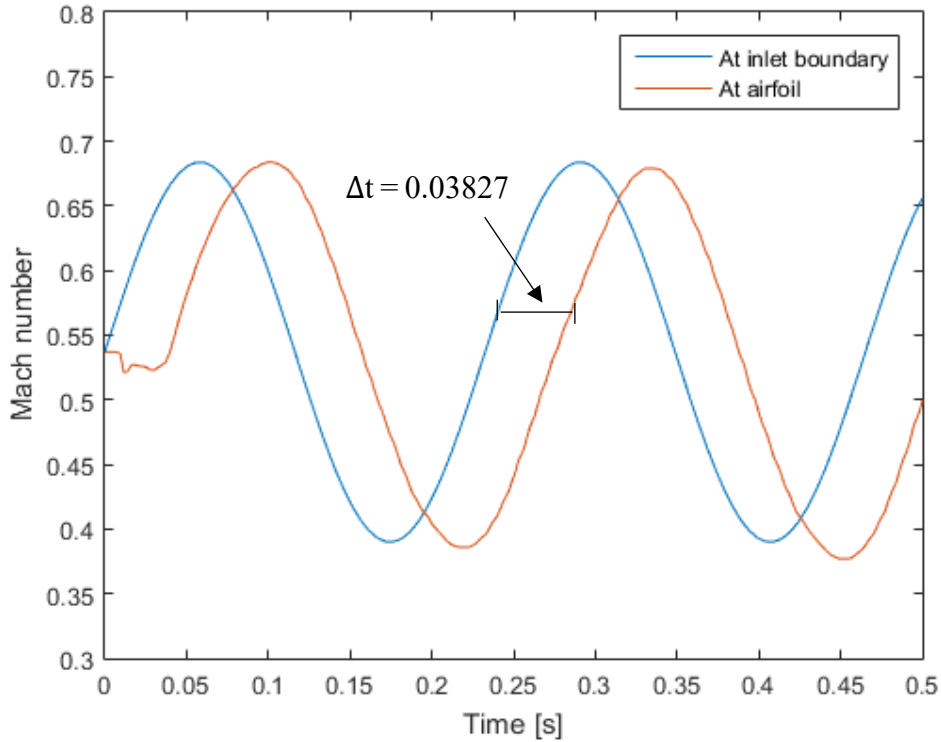


Figure 3.17: Application of time lag for unsteady freestream case.

The calculated time lag was then applied to the airfoil pitching equation as shown in Equation 3.2. The addition of the time lag ensures the correct coupling of instantaneous velocity and angle of attack.

$$AOA(t) = AOA_{mean} + AOA_{amp} * \sin\{\omega(t - t_{lag})\} \quad (3.2)$$

3.2.3.4 Cycle Periodicity Convergence

As in the constant freestream case, the simulation was run for four cycles to determine when periodicity would be achieved in the aerodynamic data. As seen in Figure 3.18, periodicity was observed after two cycles. The data shown in Figure 3.18 is the lift and moment non-dimensionalized by the average velocity rather than the instantaneous velocity. The anomalies seen in the beginning of the first cycle come from the application of the time lag, i.e. the correct freestream velocity has not reached the airfoil yet.

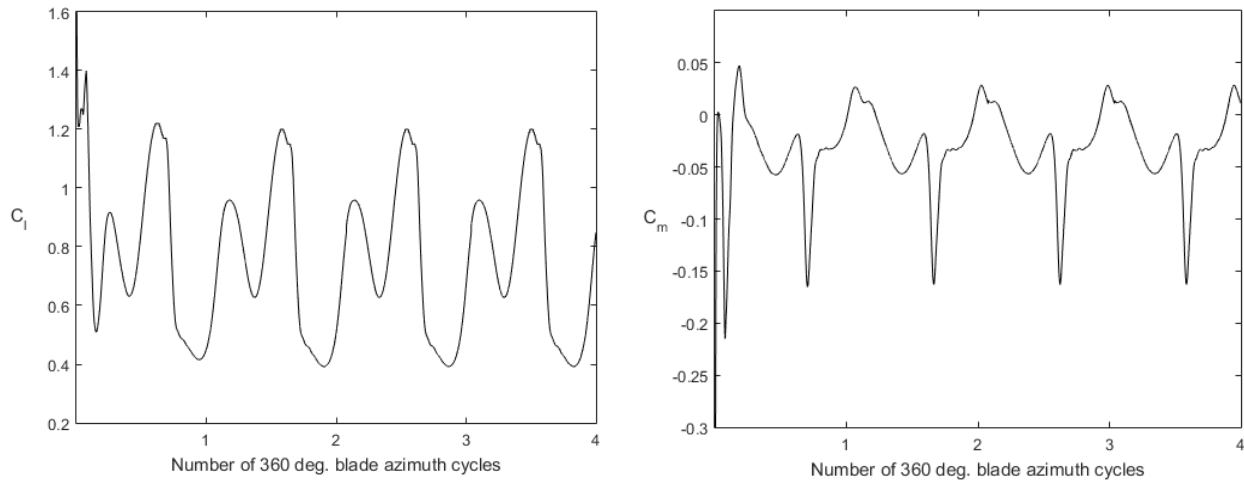


Figure 3.18: Time history of aerodynamic loads for unsteady freestream case.

3.3 Utilization of Dynamic Stall Aerodynamic Data in Qoptr

The hysteretic behaviour of dynamic stall aerodynamic data requires a different aerodynamic coefficient assignment algorithm than when only steady aerodynamic data is used. As part of this thesis work, a dynamic stall module was added to *Qoptr* to improve its forward flight analysis capabilities. The development and implementation of the module is discussed in the following sections.

3.3.1 Characteristics of Dynamic Stall Aerodynamic Data

In the context of rotor analysis, the hysteresis loop seen in dynamic stall aerodynamic data is the most important feature. In the down-stroke phase, where the angle of attack is decreasing, the aerodynamic data is significantly different from what it was in the up-stroke phase at the same angles of attack as seen in Figure 3.19.

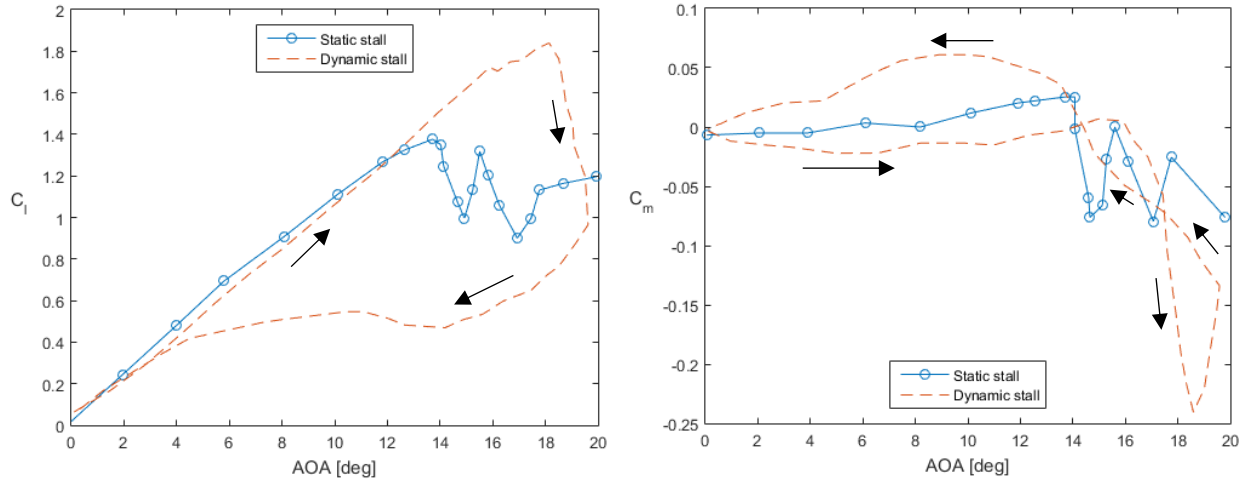


Figure 3.19: Hysteretic aerodynamic behaviour of dynamic stall on NACA 0012 (adapted from Ref. [1]).

This means that the aerodynamic coefficient cannot simply be assigned to a blade section as a function of angle of attack and Reynolds/Mach number as it is in hover analysis, but also whether the blade section is in up-stroke or down-stroke phase has to be considered.

3.3.2 Aerodynamic Data Look-up Table Organization in *Qoptr*

In Blade Element Momentum Theory (BEMT) based rotor analysis codes like *Qoptr*, the 2D aerodynamic data of the airfoils are organized in the form of look-up tables. Once the local velocity and angle of attack are calculated at each blade section, appropriate aerodynamic coefficient is selected from the look-up table and gets assigned to the corresponding blade section. When only static aerodynamic data is considered, only the local velocity and angle of attack need to be known to retrieve the aerodynamic data. However, when dynamic stall aerodynamic is used, the blade azimuth also has to be considered.

3.3.2.1 Data Selection in Hover Analysis

For hover analysis in *Qoptr*, only the static aerodynamic data is used as the blade angle of attack stays constant with blade azimuth. Three data files are used per airfoil each containing lift, moment,

and drag coefficient data, and the data files contain the aerodynamic data as a function of angle of attack and Reynolds number. If the calculated velocity and/or angle of attack is out of the range of the data files, the closest available data is used.

3.3.2.2 Data Selection in Forward Flight Analysis

While static aerodynamic data is still needed for the non-stalled inboard part of the blade, dynamic stall aerodynamic data is used for the stalled outboard regions in forward flight analysis. The dynamic stall aerodynamic data is contained as a function of angle of attack and Reynolds number like the static data, but it is also divided into up-stroke and down-stroke parts – the stroke phase is illustrated in Figure 3.20. Therefore, the data selection algorithm in forward flight analysis also uses the blade azimuth location to determine the stroke phase. The flow chart in Figure 3.21 outlines the aerodynamic data selection and assignment process for forward flight analysis in Q_{opt} .

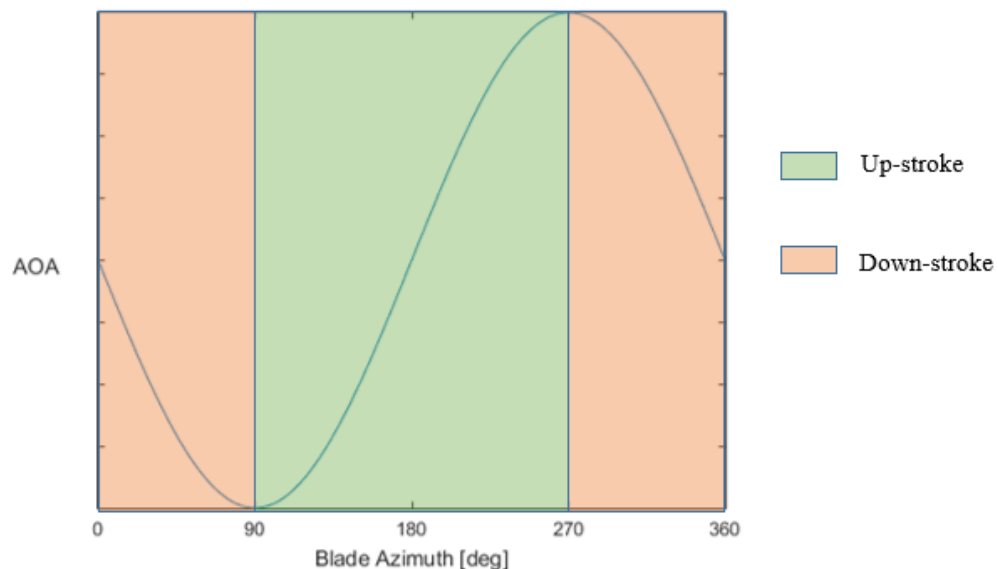


Figure 3.20: Blade angle of attack stroke phase.

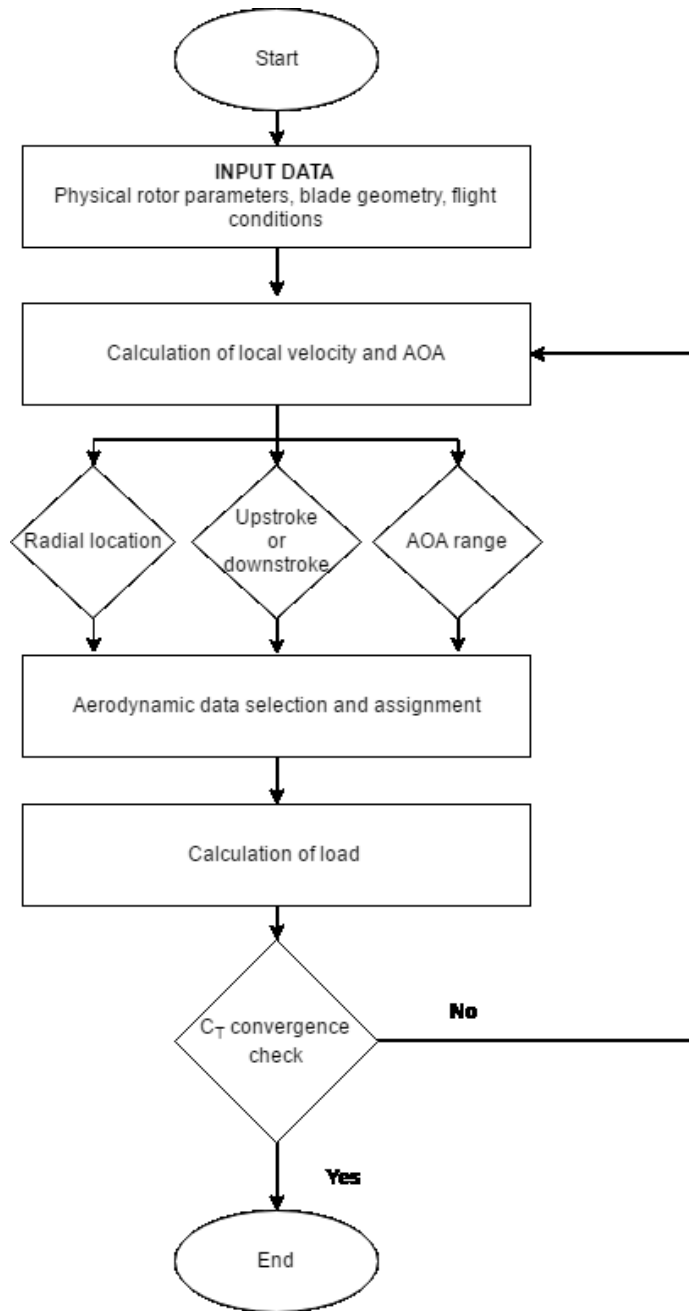


Figure 3.21: Aerodynamic data selection and assignment flowchart.

Chapter 4

Results

This chapter is structured into two sections. The first section discusses the aerodynamic data generated with CFD, observing the differences between steady and unsteady freestream dynamic stall aerodynamic data, and its sensitivity to changes in the flow conditions. In the second section, the impact of using unsteady freestream dynamic stall aerodynamic data will be discussed by looking at the blade airload results generated by *Qoptr*.

4.1 Effects of Mach Number on Dynamic Stall

In forward flight, dynamic stall takes place on the outboard region of the blades where the local Mach numbers are typically between 0.5 and 0.8. At these transonic Mach numbers, compressibility effects are significant and have a large effect on the stall behaviour of the airfoil. Generally, the stall angle decreases with increasing Mach number since the formation of a shock wave on the upper surface promotes flow separation. The effects of the Mach number on constant and unsteady freestream dynamic stall is discussed in the following sections.

4.1.1 Effects of Mach Number on Constant Freestream Dynamic Stall

The effects of Mach number on constant freestream dynamic stall was found to be similar to that of static stall. Figure 4.1 shows the lift and moment coefficient histories for a SC1094 R8 airfoil at different Mach number dynamic stall conditions. Similar to static stall, the stall angle decreased with increasing Mach number. While the aerodynamic behaviour is consistent in the attached region across the Mach numbers, the stall and down-stroke behaviours are significantly different.

The large non-linear differences seen in the aerodynamic behaviour at different Mach numbers indicate that a wide range of data at various Mach numbers is needed for accurate rotor analysis.

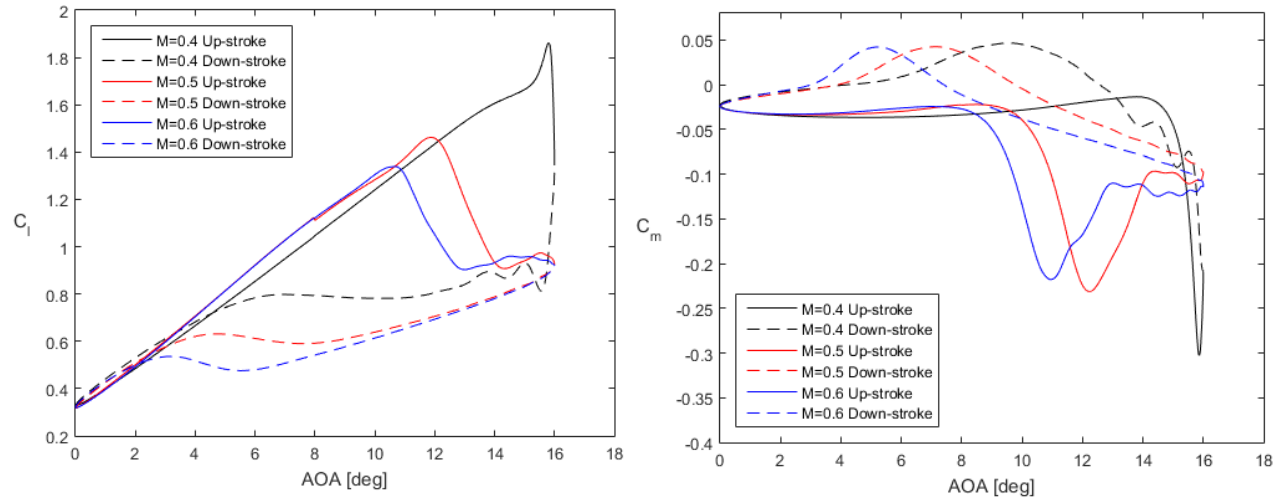


Figure 4.1: Effect of Mach number of constant freestream dynamic stall on SC1094 R8 airfoil.

Figure 4.2 shows the flow-field at 11 degree AOA under different Mach numbers. At $M = 0.4$, the flow is fully attached to the airfoil. At $M = 0.6$ however, the flow is almost fully separated.

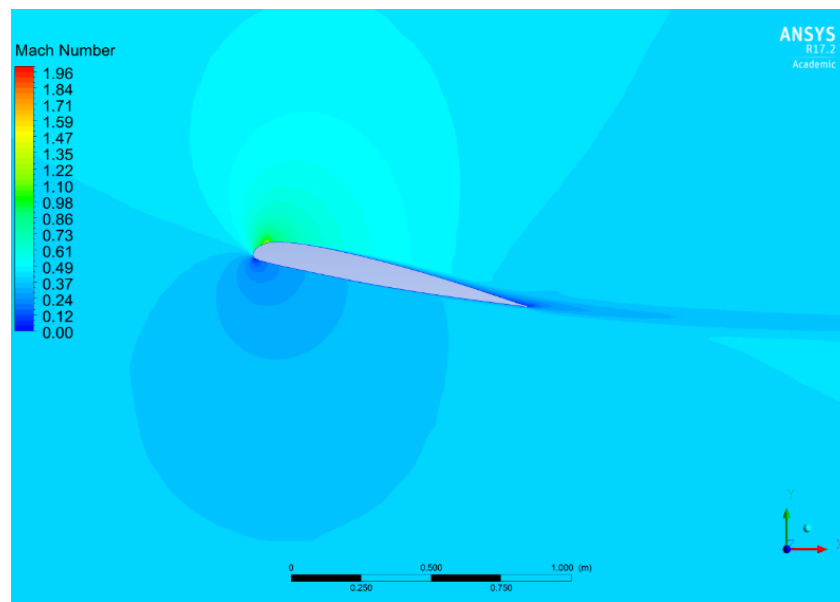


Figure 4.2: Mach number contour of SC1094 R8 airfoil at $M = 0.4$ and $\alpha = 11^\circ$.

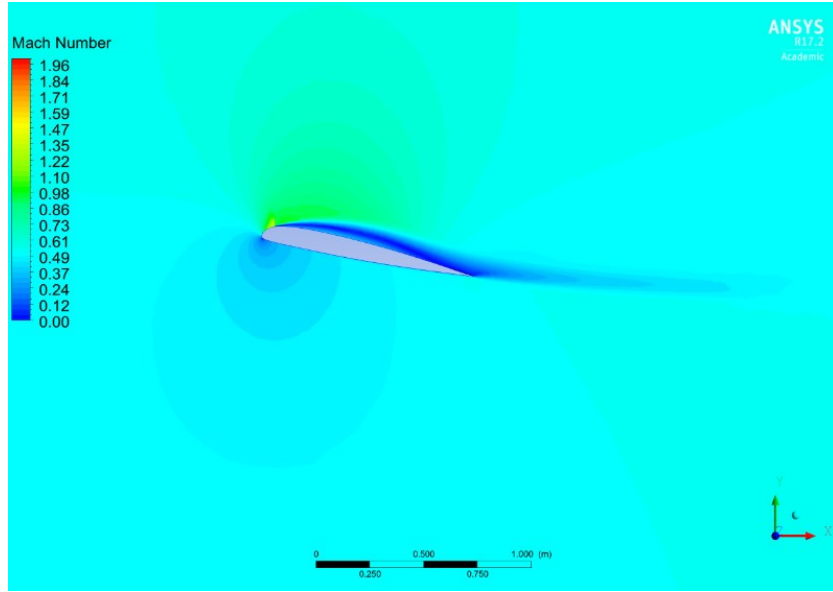


Figure 4.3: Mach number contour of SC1094 R8 airfoil at $M = 0.5$ and $\alpha = 11^\circ$.

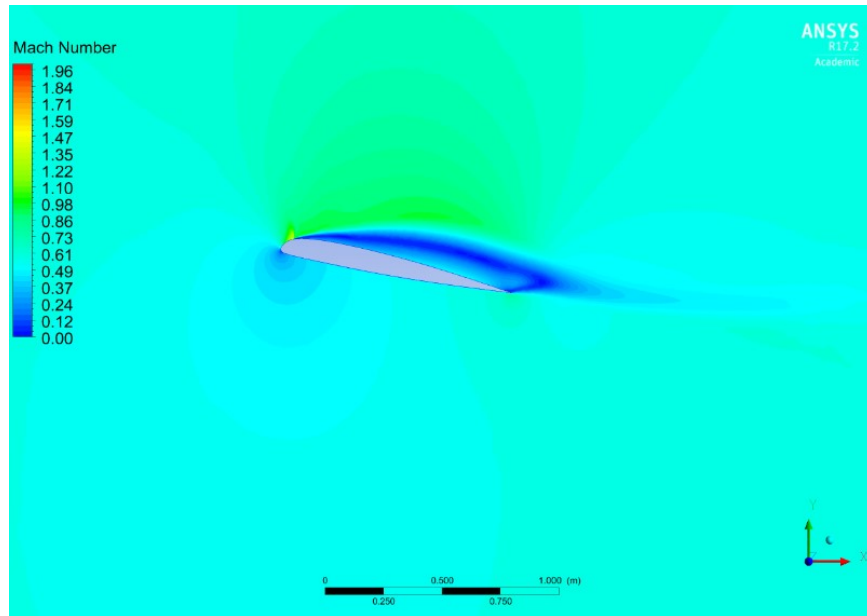


Figure 4.4: Mach number contour of SC1094 R8 airfoil at $M = 0.6$ and $\alpha = 11^\circ$.

4.2 Effects of Unsteady Freestream on Dynamic Stall

To investigate the effect of introducing unsteady freestream on dynamic stall, two dynamic stall simulations were run on the SC1094 R8 airfoil where the freestream was held constant in one, and varying sinusoidally in the other. The angle of attack was set to vary from 0 to 16° to initiate the stall process. The comparison of the lift and moment coefficients from the two cases are shown in Figures 4.5 and 4.6.

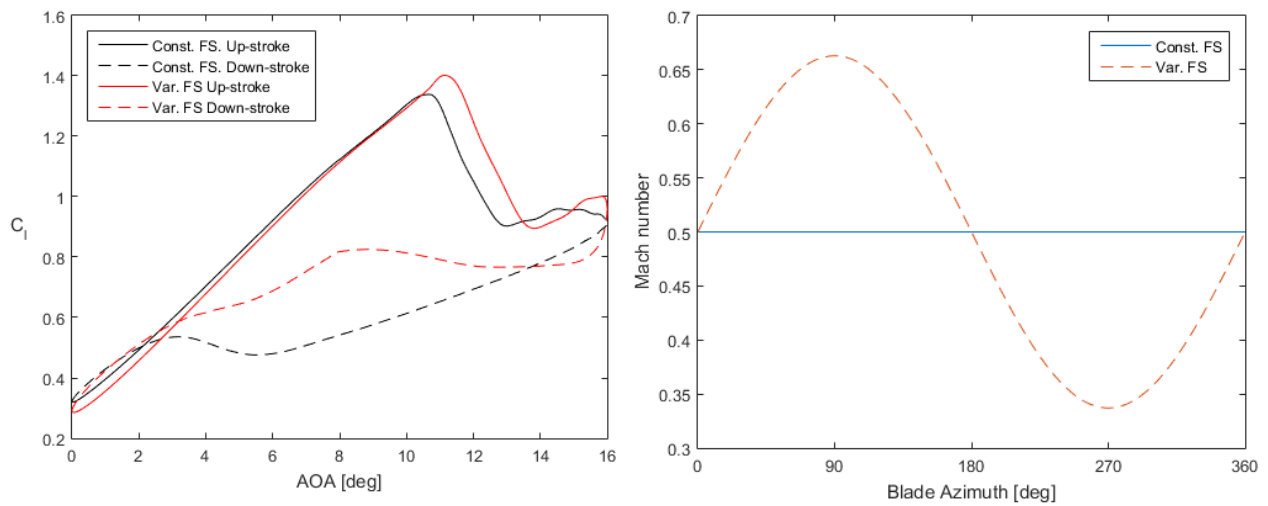


Figure 4.5: Comparison of lift coefficient from steady and unsteady freestream dynamic stall.

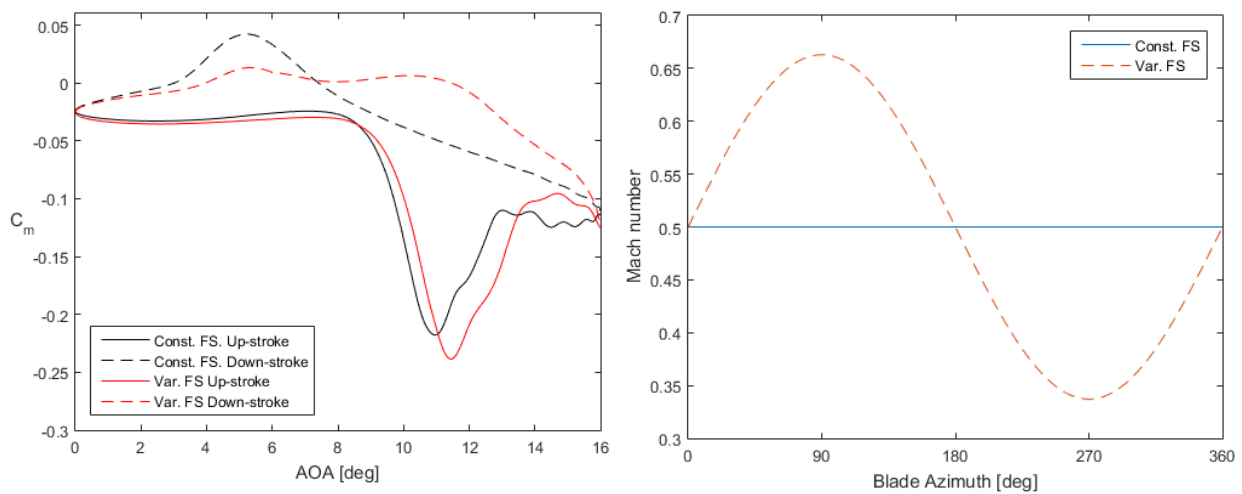


Figure 4.6: Comparison of moment coefficient from steady and unsteady freestream dynamic stall.

As seen in Figures 4.5 and 4.6, the airfoil showcased significantly different aerodynamic behaviour under the two conditions. The most notable difference is the delay of stall in the unsteady freestream case. Since the angle of attack and the freestream velocity are fluctuating 180 degrees out of phase as indicated in Figure 3.12, the airfoil sees the minimum freestream velocity at the maximum angle of attack where stall is likely to happen. Thus, the airfoil in the steady freestream case sees a higher Mach number than its counterpart in the unsteady freestream case, causing it to stall earlier at a smaller angle of attack. The different stall timing of the two cases caused them to have largely different hysteresis behaviour in the down-stroke phase.

4.3 Effects of Angle of Attack Range on Unsteady Freestream Dynamic Stall

Since the blade angle of attack range is not known prior to rotor analysis, but rather a variable that is solved iteratively during the analysis, the aerodynamic data of the blade sections must be available across various angle of attack ranges. It was found that unsteady freestream dynamic stall aerodynamic data were quite sensitive to the angle of attack range. Figure 4.7 shows the aerodynamic data for the SC1094 R8 airfoil at two different angle of attack ranges. The data in Figure 4.7 was obtained at oscillating Mach number of $M = 0.54 \pm 0.16$.

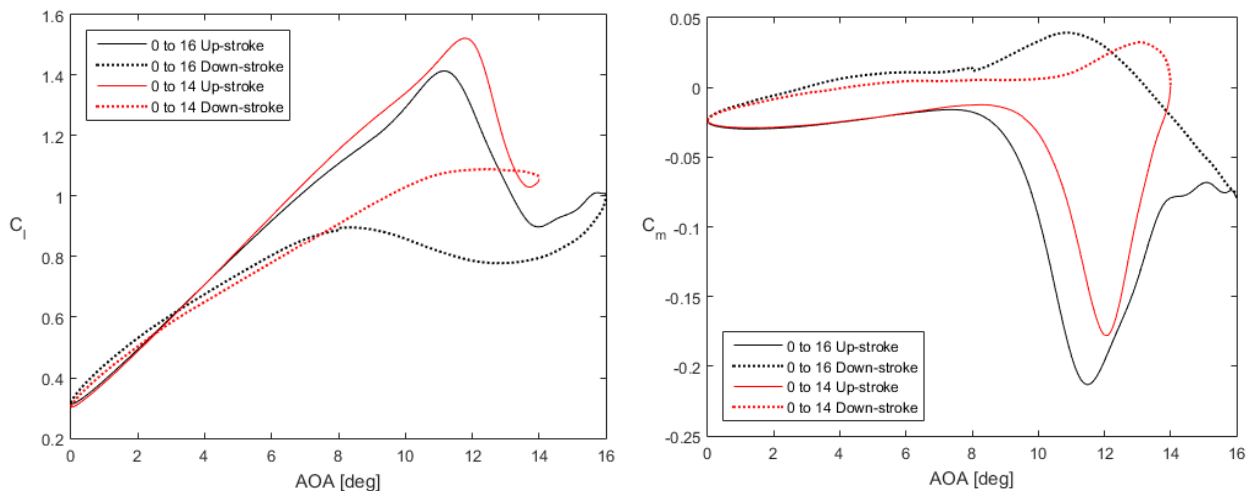


Figure 4.7: Effect of AOA range on variable freestream dynamic stall behavior on SC1094 R8.

As seen in Figure 4.7, the aerodynamic behaviour of the airfoil from the two cases is almost identical in the attached flow region as expected. However, due to the different stall timing the down-stroke behaviour is significantly different between the two cases. Since the unsteady Mach number and oscillating angle of attack are controlled by prescribed out-of-phase sinusoidal equations, a change in the angle of attack range changes the Mach number seen at a particular angle of attack affecting the stall characteristic. In the case shown in Figure 4.7, the Mach number at 12° angle of attack for the smaller angle of attack range case is about 7% lower than that of the other case at the same angle of attack. As previously shown, a small change in Mach number can have a significant effect on the stall characteristics.

4.4 *Qoptr* Results with Constant Freestream CFD Dynamic Stall Data

Although the main goal of this thesis was to investigate the impact of using variable freestream dynamic stall data for forward flight analysis, it is also worthwhile to see if using constant freestream dynamic stall data generated with CFD can yield more accurate results than the semi-empirical dynamic stall models. Since constant freestream CFD dynamic stall simulations are less complex and require less computational resources than the variable freestream cases, they could be an attractive method for preliminary analysis. As seen in Figure 4.8, CFD showed a higher accuracy than the semi-empirical models under realistic flow conditions and reduced frequency. The data shown in Figure 4.8 were obtained at $M = 0.301$ and at $k = 0.1$.

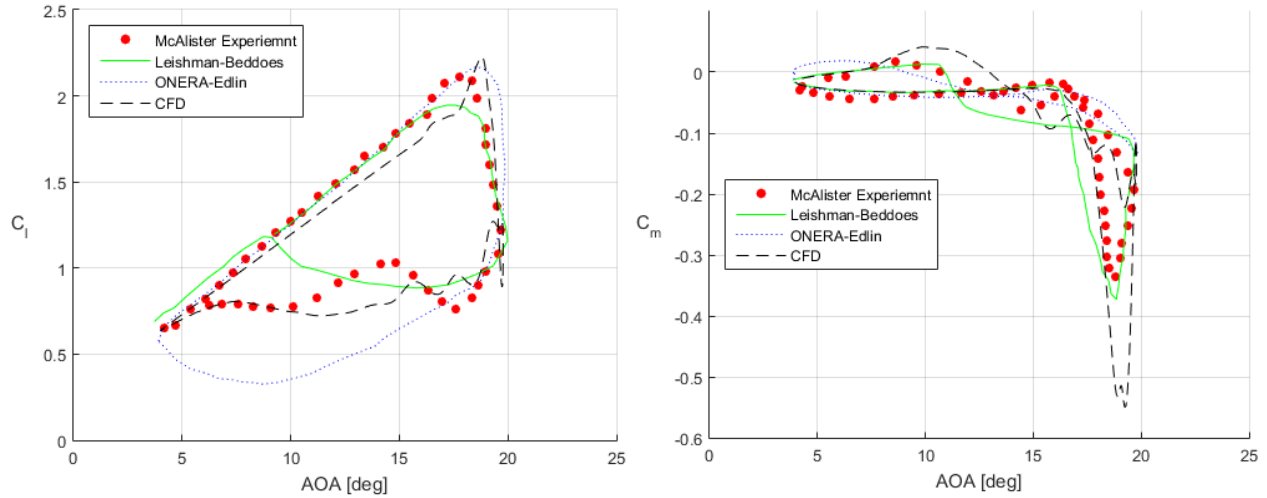
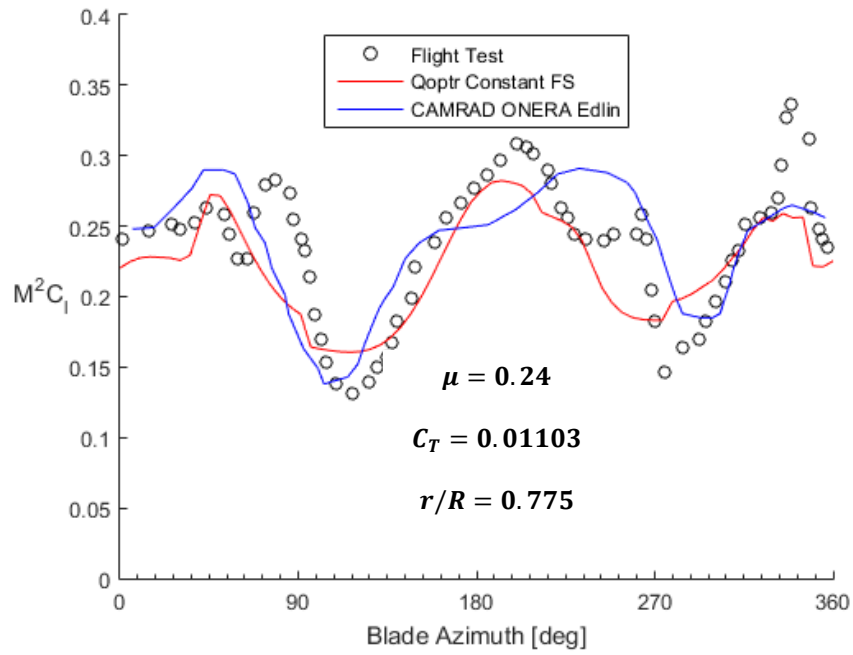
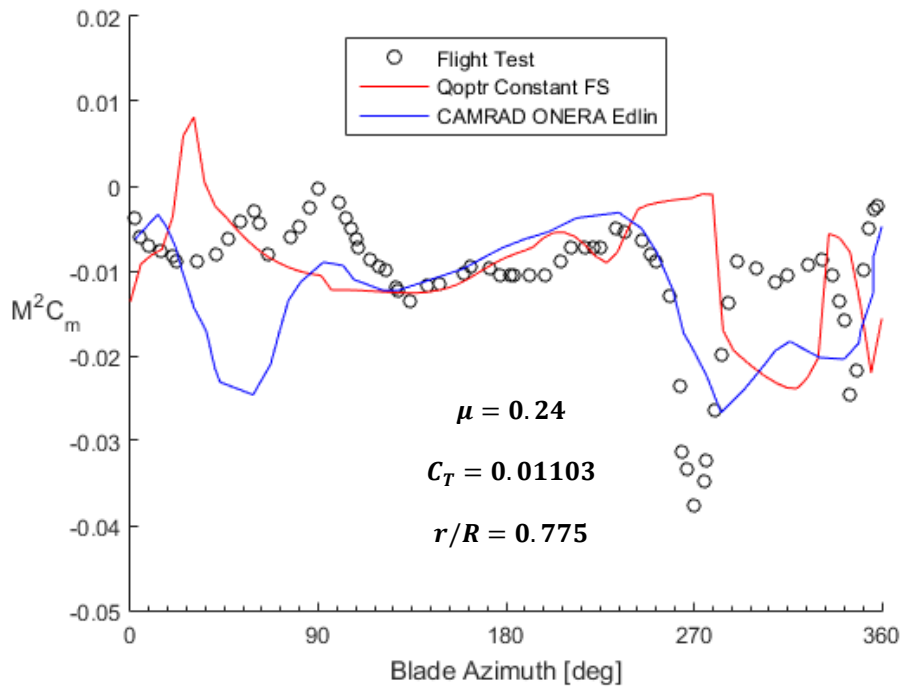


Figure 4.8: Comparison of constant freestream CFD dynamic stall data to semi-empirical dynamic stall model results.

Under the UH-60A validation flight conditions of $\mu = 0.24$ and $C_T = 0.0110$, dynamic stall occurs on the outboard region of the blade at $r/R \geq 0.55$. At $r/R \geq 0.55$, and the Mach number roughly ranges from 0.4 and 0.8. Therefore, constant freestream dynamic stall data were generated at these Mach numbers at an increment of M 0.1 at angle of attack ranges of $0^\circ - 14^\circ$ and $0^\circ - 16^\circ$. With this available aerodynamic data, Q_{opt} was used to calculate the blade airloads under the same conditions as the UH-60A validation case. The comparison of the Q_{opt} results to the flight test data is shown in Figure 4.9.



(a)



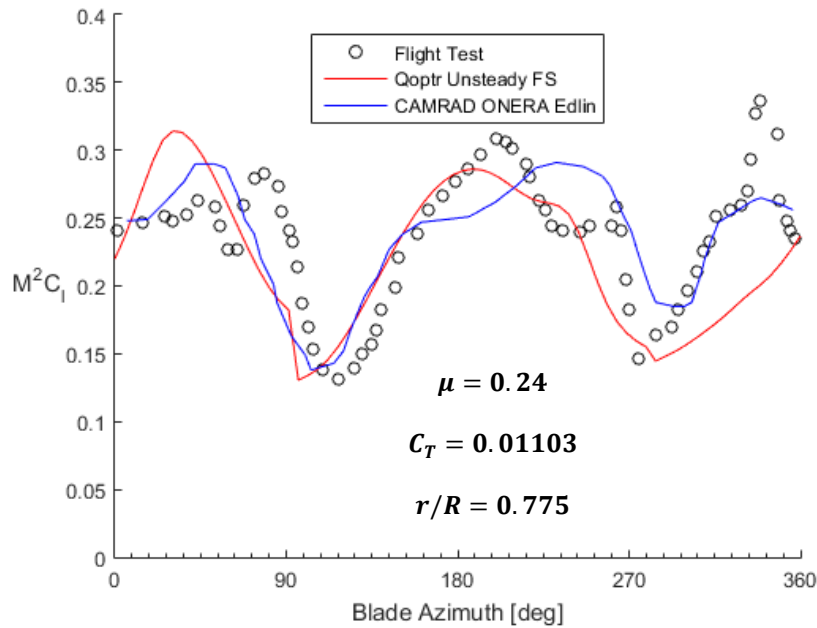
(b)

Figure 4.9: Comparison of constant freestream DS Qoptr results to flight test data.

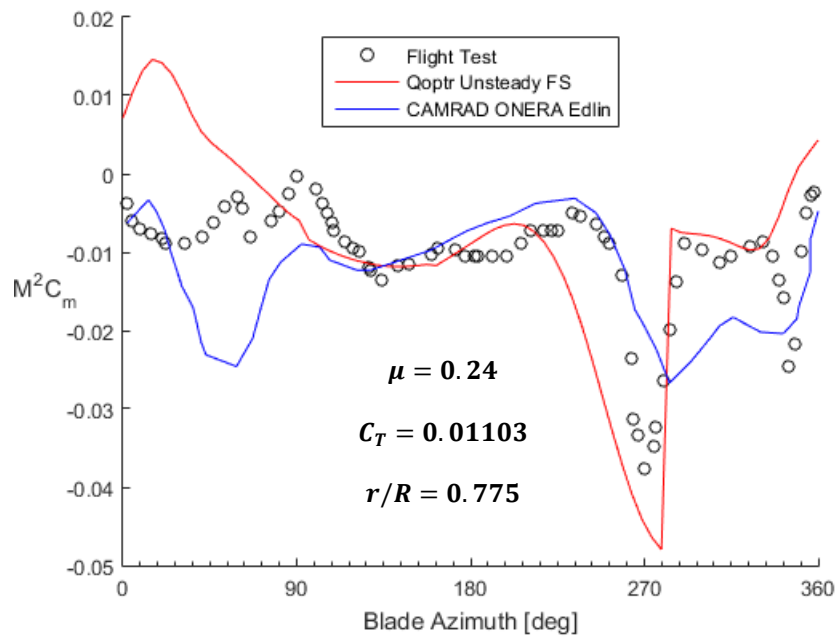
As shown in Figure 4.9 (a), the section lift history was predicted quite well by *Qoptr*. The general trend was well captured and the magnitude was also predicted with respectable accuracy. For the section pitching moment history shown in Figure 4.9 (b), the *Qoptr* results showed lower accuracy than the section lift history. Although the general trend is partially captured, the peak at 270-degree blade azimuth was not captured well. Overall, the *Qoptr* results showed a similar level of accuracy as the results generated with CAMRAD II with the ONERA EDLIN dynamic stall model, substantiating the fact that the exclusion of the unsteady freestream in the semi-empirical models is at least partly responsible for the inaccuracy.

4.5 *Qoptr* Results with Unsteady Freestream CFD Dynamic Stall Data

For the forward flight analysis with unsteady freestream CFD dynamic stall data, the aerodynamic data were generated with the flow conditions representative of four radial locations, $r/R = 0.6$, $r/R = 0.7$, $r/R = 0.8$, and $r/R = 0.9$. The aerodynamic data were gathered for two different angle of attack ranges of 0° to 14° and 0° to 16° . Figure 4.10 shows the blade airload results generated with *Qoptr* using unsteady freestream dynamic stall data.



(a)



(b)

Figure 4.10: Comparison of unsteady freestream DS Qoptr results to flight test data.

Overall, the agreement between the flight test data and the numerical results is respectable. The section lift history was captured well throughout the azimuth, and the agreement between the flight

test data and the *Qoptr* results improved for the section pitching moment history. Compared to the results generated with semi-empirical models and constant freestream CFD dynamic stall data, where both the location and the magnitude of the peak was predicated inaccurately, the results generated with unsteady freestream CFD dynamic stall data predicted the peak significantly better. Since stall characteristics are largely dependent on the freestream Mach number, the improvement in the accuracy of the blade airload prediction near the 270-degree blade azimuth where the maximum angle of attack is achieved is logical.

4.5.1 Factors Influencing Solution Accuracy

Although the overall accuracy and the prediction of stall have increased for both lift and pitching moment history, a considerable error exists around 0-degree blade azimuth. This error is likely caused by the fact that the aerodynamic behavior of the blade section is highly sensitive to the angle of attack range as discussed in section 4.3. The blade azimuth angles where the largest error is overserved, i.e. $\sim 0^\circ$ to 45° and $\sim 270^\circ$ to 360° , fall under the high angle of attack region in the down-stroke phase. Figure 4.11 shows this correlation by colour.

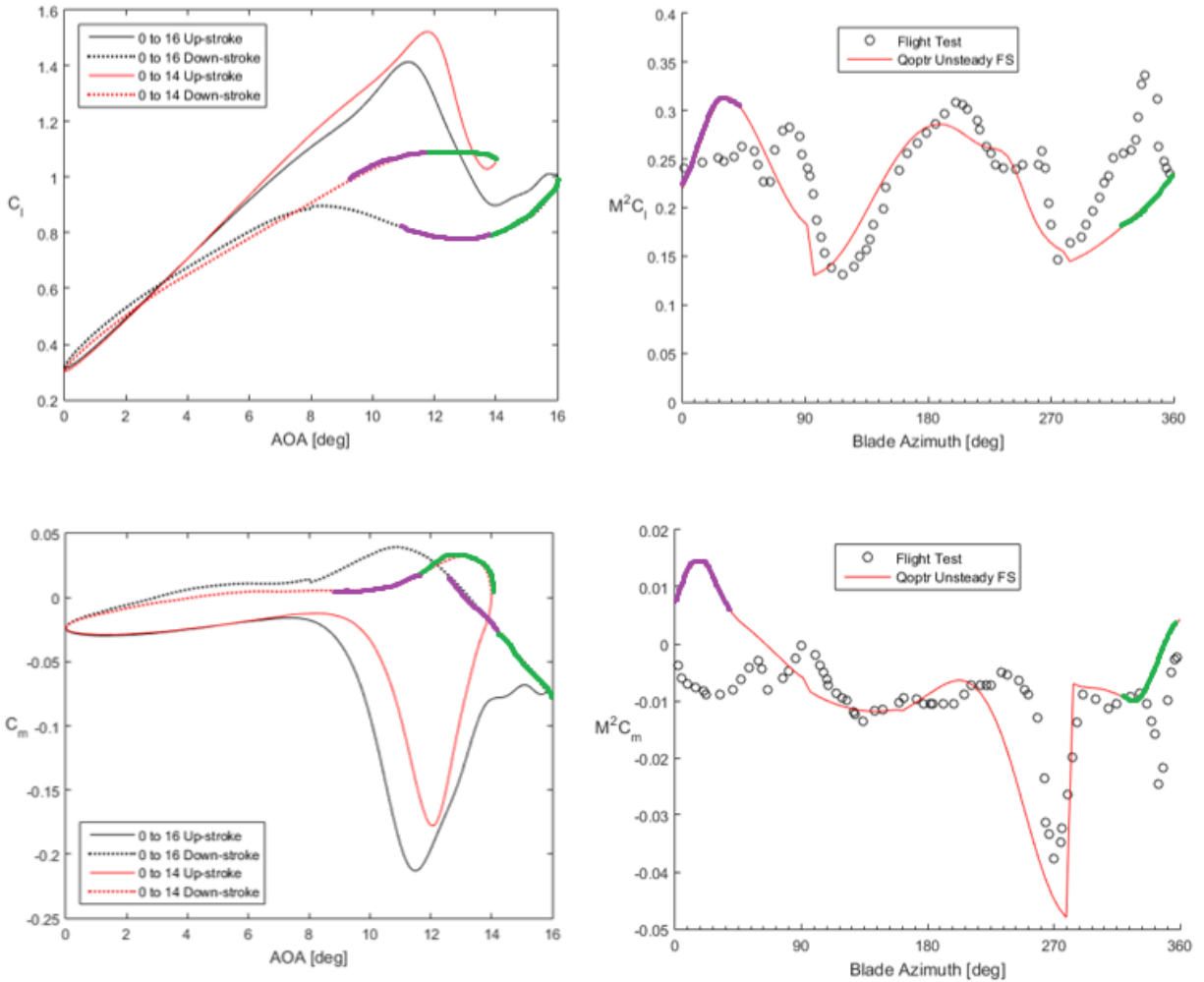


Figure 4.11: Effect of angle of attack range sensitivity on solution accuracy at $r/R = 0.775$.

As seen in Figure 4.11, the aerodynamic data is most sensitive to the angle of attack range at the locations where the largest error is observed. Since the aerodynamic data were generated only at three different angle of attack of ranges, it is likely that the error near the 0-degree blade azimuth was partly caused by inaccurate high angle of attack down-stroke aerodynamic data.

In a recent study at ONERA, Richez [42] studied dynamic stall on a helicopter rotor in forward flight with 3D CFD. In his study, the entirety of the rotor was modelled in 3D, and a CFD solver coupled with a comprehensive code was used to solve the flow field. Richez investigated two dynamic stall conditions and compared the CFD blade airload results to the wind tunnel rotor test

data. Although the rotor geometry and the dynamic stall conditions used in his study are not identical to that of the UH-60A validation case used in this work, it is interesting to see that similar errors were observed in his results as seen in Figure 4.12.

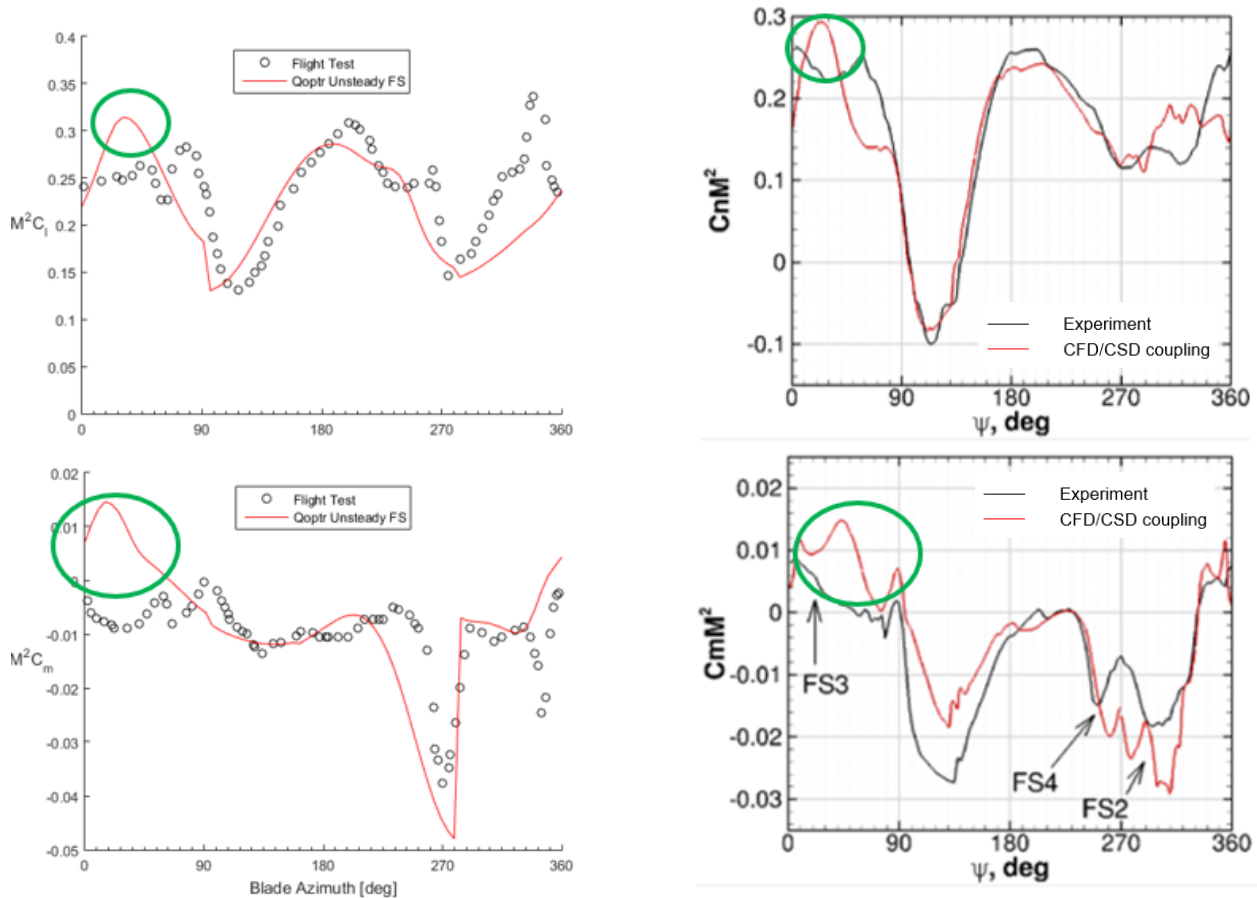


Figure 4.12: Airload prediction error in full 3D CFD rotor simulation [42].

Richez's results on the right were obtained at $r/R = 0.925$, but the mean Mach number at this location is similar to the mean Mach number of the UH-60A validation case at $r/R = 0.775$, therefore the two cases share similar flow physics.

In his paper, Richez speculated that a separation bubble that he observed on the outboard region near the 0-degree blade azimuth was responsible for the fluctuation in the section pitching moment

results as seen in Figure 4.12. Interestingly, a separation bubble was also observed in the unsteady freestream dynamic stall simulation of the UH-60A blade section as illustrated in Figure 4.13. It is likely that this shock-induced separation bubble was also responsible for the overprediction of the first peak in the section lift results.

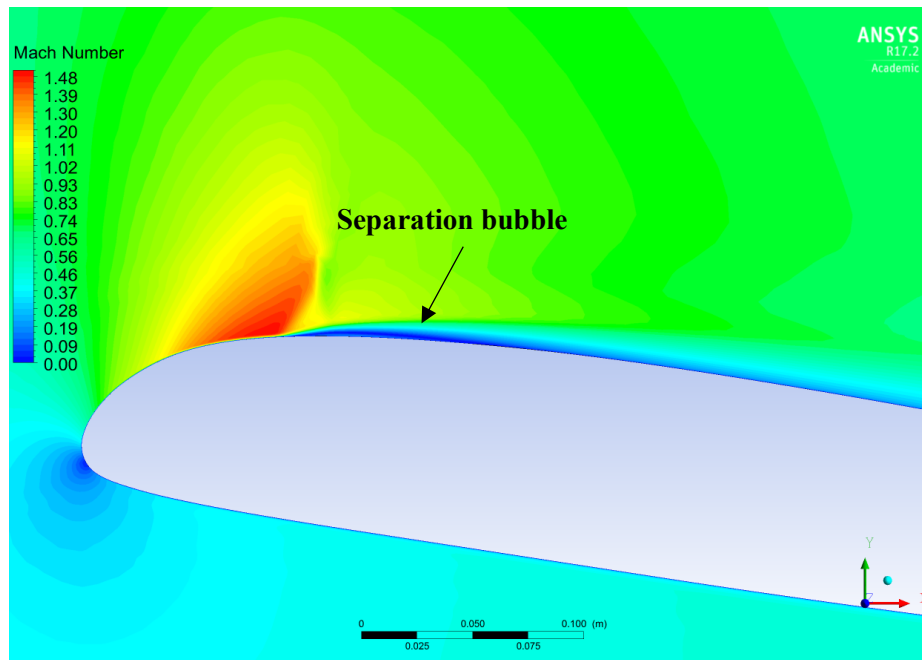
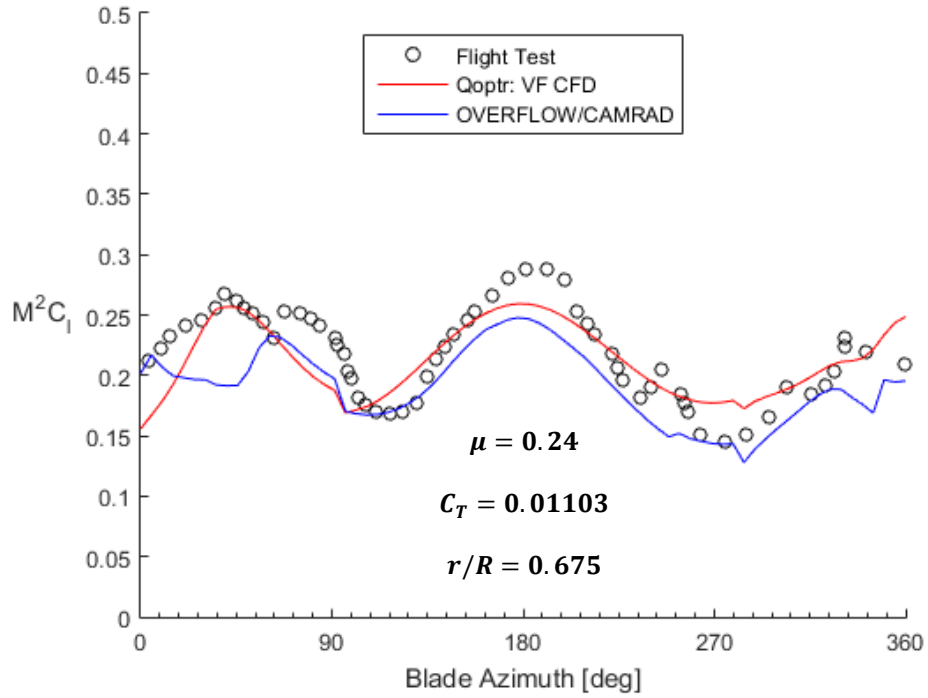


Figure 4.13: Separation bubble formation during down-stroke phase.

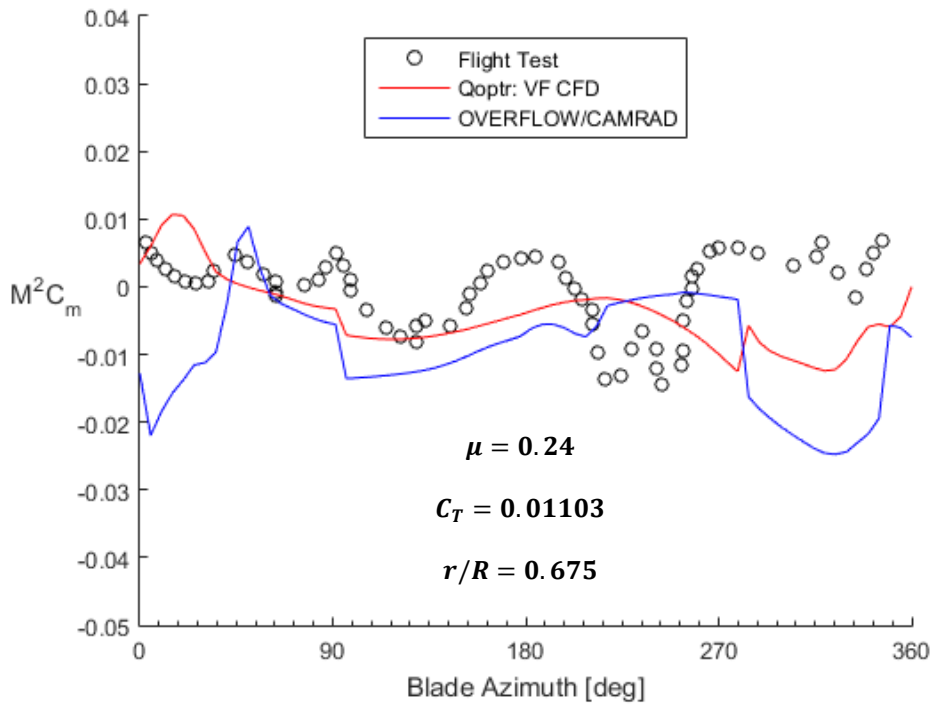
4.5.2 Blade Airload Results at Other Radial Positions

While the availability of CAMRAD II blade airload results generated with semi-empirical models made radial position of $r/R = 0.775$ an ideal location for the purposes of this research, it is also important to look at the results at other radial locations. The other two radial positions often considered in other work are $r/R = 0.675$ and $r/R = 0.865$. At these locations, both lift stall and moment stall take place as indicated in the dynamic stall rotor map in Figure 2.5. Therefore, good prediction of the blade airloads at these radial locations is important for accurate forward flight analysis. Figures 4.14 and 4.15 show the blade airload results at $r/R = 0.675$ and $r/R = 0.865$,

respectively. In the absence of CAMRAD II results generated with semi-empirical dynamic stall models, results generated with 3D CFD coupled with computational structural dynamics (CSD) by Potsdam et al. [43] are shown for comparison.

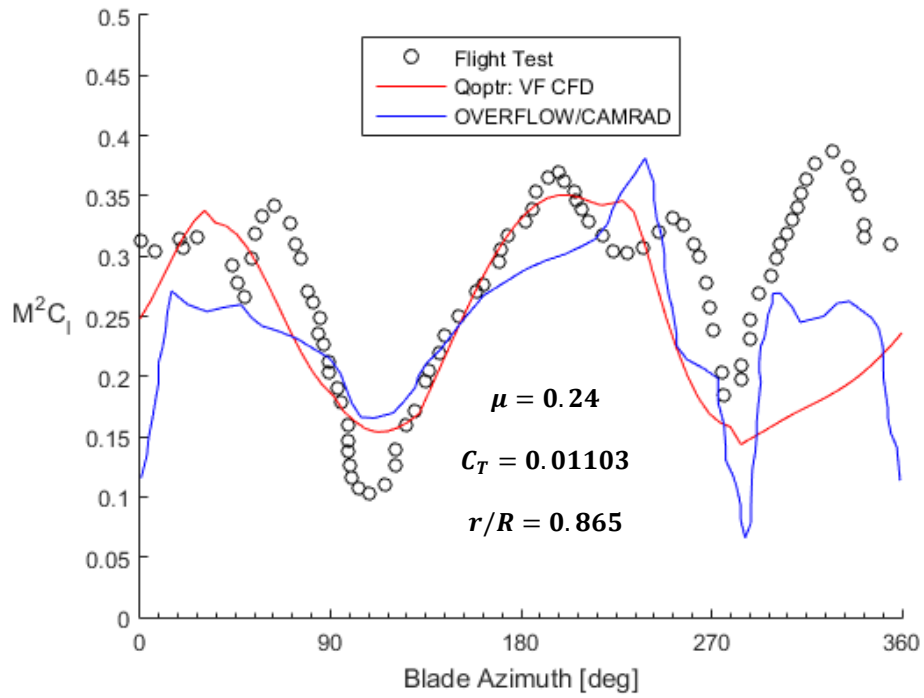


(a)

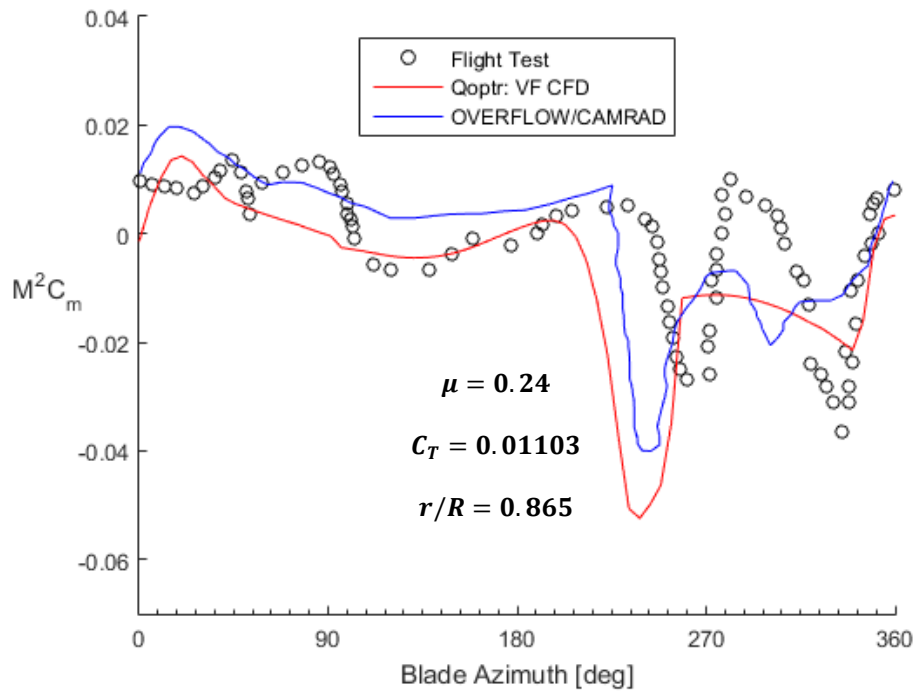


(b)

Figure 4.14: Qoptr blade airload results at $r/R = 0.675$.



(a)



(b)

Figure 4.15: Qoptr blade airload results at $r/R = 0.865$.

At $r/R = 0.675$, the section lift was predicted very well by *Qoptr*. In fact, it shows better accuracy than the much more computationally expensive 3D CFD method coupled with CSD. For the section pitching moment, neither method provide satisfactory results. Both methods showed a large error between 270 and 360-degree azimuth. As discussed in section 4.5.1, the error shown in the *Qoptr* results is likely from the angle of attack range sensitivity.

A similar statement can be made about the results at $r/R = 0.865$. The section lift was predicted well with the exception of azimuth angles between 270 and 360 degrees. The section pitching moment was predicted better at this radial location. Though the magnitude and the location were slightly off, the two stall events were captured; the first one near 270-degree azimuth and the second near 330-degree azimuth.

Overall, the *Qoptr* results generated with unsteady freestream CFD dynamic stall data showed respectable accuracy. For this particular flight condition and at these radial positions, they show better agreement with the flight test data than the results generated with more complex and computationally expensive coupled method.

Chapter 5

Conclusions and Recommendations

5.1 Conclusions and Accomplishments

In this work, the impact of using CFD dynamic stall data obtained at time-varying freestream on the accuracy of forward flight blade airload prediction was investigated. The time-varying or unsteady freestream dynamic stall aerodynamic data was obtained via Fluent, a commercial URANS CFD code, and in-house rotor analysis code *Qoptr* was used to calculate the blade airloads using the generated CFD data. Flight test blade airload data obtained at $C_T/\sigma = 0.129$ and $\mu = 0.24$ from NASA's UH-60A Airload program was used to evaluate the accuracy of the *Qoptr* results.

Qoptr results generated with time-varying freestream dynamic stall aerodynamic data showed better agreement with the flight test data than the CAMRAD II results generated with various semi-empirical models such as Leishman-Beddoes and ONERA EDLIN models at $r/R = 0.775$. The largest improvement was seen in the pitching moment peak where both the magnitude and the location of the peak was predicted better by *Qoptr*. Results at other radial locations ($r/R = 0.675$ and $r/R = 0.865$) showed good agreement with the flight test data as well showing higher accuracy than the coupled CFD and CDS method at some blade azimuth angles.

Likely sources of error of this method were also investigated. While the overall accuracy and the prediction of the main stall event improved, considerable errors were observed near the 0-degree blade azimuth. It was found that the sensitivity of dynamic stall aerodynamic data to the angle of attack range was a probable cause. Around the 0-degree blade azimuth position, the blade section

is at a high angle of attack in the down-stroke phase, thus its aerodynamic behaviour is largely affected by the angle of attack range. Also, the separation bubble observed in the CFD simulation during the down-stroke phase likely has artificially increased the lift and positive pitching moment.

5.2 Recommendations for Future Work

The findings of this research suggest that neglecting the unsteady nature of the freestream velocity in helicopter forward flight is partly responsible for the discrepancy between the flight test blade airload data and numerical results with conventional rotor analysis methods. However, in this study only one flight condition was considered and investigated. The importance of the inclusion of time-varying freestream in dynamic stall modelling should be more thoroughly understood by considering different flight conditions where different “depths” of dynamic stall are considered.

The availability of the aerodynamic data obtained at various flow conditions is crucial for accurate rotor analysis. Creating a large database of dynamic stall aerodynamic data for the SC1095 and SC1094 R8 airfoils would allow more accurate analysis of UH-60A forward flight. The availability of its flight test data from the UH-60A Airloads program can be utilized for further validation of rotor analysis codes.

For more high-fidelity validation, more detailed modelling of the rotor blades should be considered. The test helicopter in the UH-60A Airloads Program was fitted with experimental blades that are equipped with a large number of pressure transducers and strain gauges. Therefore, the actual blade profile may be different enough than the “clean” blade profile that most rotor analysis codes would assume causing different aerodynamic behaviour.

References

- [1] J. G. Leishman, "Principles of Helicopter Aerodynamics", 2nd ed., Cambridge, U.K., 2006.
- [2] G. B. McCullough and D. E. Gault, "Examples of three representative types of airfoil-section stall at low speed," NACA, Moffett Field, Technical note 2502, 1951.
- [3] P. Gerontakos, "Unsteady Airfoil Flow Control via a Dynamically Deflected Trailing-Edge Flap, Ph.D Dissertation," McGill University, Montreal, Canada , 2008.
- [4] W. McCroskey, "Inviscid Flowfield of an Unsteady Airfoil," *AIAA Journal*, vol. 11, no. 8, pp. 1130-1136, 1973.
- [5] T. Beddoes, "Onset of Leading Edge Separation Effects under Dynamic Conditions and Low Mach Number," in *34th Annual Forum of the American Helicopter Society*, Washington DC, May 15-17, 1978.
- [6] W. G. Bousman, "A Qualitative Examination of Dynamic Stall from Flight Test Data," *Journal of the American Helicopter Society* , vol. 43, no. 4, pp. 284-286, 1998.
- [7] W. Johnson, "Rotorcraft Aerodynamics Models for a Comprehensive Analysis," in *American Helicopter Society 54th Annual Forum*, Washington DC, May 20-22, 1998.
- [8] W. G. Bousman, "Rotorcraft Airloads Measurements: Extraordinary Costs, Extraordinary Benefits," *Journal of the American Helicopter Society* , vol. 59, no. 3, pp. 1-30, 2014.

- [9] F. Tarzanin, "Prediction of Control Loads Due to Blade Stall," *Journal of the American Helicopter Society*, vol. 17, no. 2, pp. 33-46, 1972.
- [10] W. J. McCroskey and R. K. Fisher, "Detailed Aerodynamic Measurements on a Model Rotor in the Blade Stall Regime," *Journal of the American Helicopter Society*, vol. 17, no. 1, pp. 22-30, 1972.
- [11] K. W. McAlister, S. L. Pucci, W. J. McCroskey and L. W. Carr, "An Experimental Study of Dynamic Stall on Advanced Airfoil Sections, Volume 2. Pressure and Force Data," NASA, NASA Technical Memorandum 84245, 1982.
- [12] K. Richter, A. Le Pape, T. Knopp, M. Costes, V. Gleize and A. D. Gardner, "Improved Two-Dimensional Dynamic Stall Prediction with Structured and Hybrid Numerical Methods," *Journal of the American Helicopter Society*, vol. 56, no. 4, pp. 1-12, 2011.
- [13] K. Al_Jaburi and D. Feszty, "Passive Flow Control of Dynamic Stall via Surface-based Trapped Vortex Generators," in *73rd Annual Forum of the American Helicopter Society*, Fort Worth, TX, May 9-11, 2017.
- [14] A. Klein, T. Lutz, E. Kramer, K. Richter, A. D. Gardner and A. R. Altmikus, "Numerical Comparison of Dynamic Stall for Two-Dimensional Airfoils and an Airfoil Model in the DNW-TWG," *Journal of the American Helicopter Society*, vol. 57, no. 4, pp. 1-13, 2012.
- [15] J. Blazek, *Computational Fluid Dynamics: Principles and Applications*, United Kingdom: Elsevier Science Ltd, 2001.

- [16] D. Gosselin and D. Feszty, "Numerical investigation of the effect of shock-induced flow separation on dynamic stall in time-varying freestream conditions," in *72nd Annual Forum of the American Helicopter Society*, West Palm Beach, Florida, May 17-19, 2016.
- [17] G. A. Pierce, D. L. Kunz and J. B. Malone, "Effect of varying freestream velocity on airfoil dynamic stall characteristics," *Journal of the American Helicopter Society*, vol. 23, no. 2, pp. 27-33, 1978.
- [18] C. A. Maresca, D. J. Favier and J. M. Rebont, "Unsteady Aerodynamics of An Aerofoil At High Angle Of Incidence Performing Various Linear Oscillations In A Uniform Stream," *Journal of the American Helicopter Society*, vol. 26, no. 2, pp. 40-45, 1981.
- [19] M. Brendel and T. J. Mueller, "Features of Transitional Separation Bubbles in an Oscillating Freestream", Forum on Unsteady Flow Separation," in *ASME Applied Mechanics, Bioengineering and Fluids Engineering Conference*, Cincinnati, Ohio, 1987.
- [20] D. Favier, A. Agnes, C. Barbi and C. Maresca, "Combined Translation/Pitch Motion: A New Airfoil Dynamic Stall Simulation," *Journal of Aircraft*, vol. 25, no. 9, pp. 805-814, 1988.
- [21] R. H. Ellsworth and T. J. Mueller, "Airfoil boundary layer measurements at low Re in an accelerating flow from a nonzero velocity," *Experiments in Fluids*, vol. 11, no. 6, pp. 368-374, 1991.
- [22] D. Favier, J. Belleudy and C. Maresca, "Influence of Coupling Incidence and Velocity Variations on the Airfoil Dynamic Stall," in *AHS 48th Annual Forum*, Washington DC, June 3-5, 1992.

- [23] Z. Shi and X. Ming, "Effects of Unsteady Freestream on Aerodynamic Characteristics of Pitching Delta Wing," *Journal of Aircraft*, vol. 45, no. 11, pp. 2182-2185, 2008.
- [24] Z. Shi and X. Ming, "Experimental Investigation on a Pitching Motion Delta Wing in Unsteady Freestream," *Modern Physics Letters B*, vol. 23, no. 3, pp. 409-412.
- [25] K. Gompertz, C. D. Jensen, J. W. Gregory and J. P. Bons, "Compressible dynamic stall mechanisms due to airfoil pitching and freestream mach oscillations," in *68th AHS International Annual Forum*, Fort Worth, TX, May 1-3, 2012.
- [26] W. Kerstens and D. R. Williams, "Energy exchange measurements with a longitudinally oscillating flow and a vertically oscillating wing," in *50th AIAA Aerospace Sciences Meeting including the New Horizons Forum and Aerospace Exposition*, Nashville, TN, 2012.
- [27] M. Kerho, "Adaptive Airfoil Dynamic Stall Control," *Journal of Aircraft*, vol. 44, no. 4, pp. 1350-1360, 2007.
- [28] G. Martinat, M. Braza, G. Harran, A. Sevrain, G. Tzabiras, Y. Hoarau and D. Favier, "Dynamic Stall of a Pitching and Horizontally Oscillating Airfoil," in *IUTAM Symposium on Unsteady Separated Flows and their Control*, 2009.
- [29] K. Gharali and D. A. Johnson, "Dynamic stall simulation of a pitching airfoil under unsteady freestream velocity," *Journal of Fluids and Structures*, vol. 42, pp. 228-244, 2013.
- [30] W. Johnson, "A History of Rotorcraft Comprehensive Analyses," in *69th Annual Forum of the American Helicopter Society*, Phoenix, AZ, May 21-23, 2013.

- [31] W. Johnson, "Rotorcraft Aerodynamics Models for a Comprehensive Analysis," in *54th Annual Forum of the American Helicopter Society*, Washington DC, May 20-22, 1998.
- [32] K. Nguyen and W. Johnson, "Evaluation of Dynamic Stall Models with UH-60A Airloads Flight Test Data," in *54th Annual Forum of the American Helicopter Society*, Washington, DC, May 20-22, 1998.
- [33] J. G. Leishman and T. S. Beddoes, "A Semi-Empirical Model for Dynamic Stall," *Journal of the American Helicopter Society*, vol. 34, no. 3, pp. 3-17, 1989.
- [34] D. Petot, "Differential Equation Modeling of Dynamic Stall," *La Recherche Aerospatiale*, 1990.
- [35] W. G. Bousman and R. M. Kufeld, "UH-60A Airloads Catalog," NASA, NASA/TM-2005-212827, 2005.
- [36] J. Wiebe, "Development of a Simulation and Optimization Framework for Improved Aerodynamic Performance of R/C Helicopter Rotor Blades," M.A.Sc. Thesis, Carleton University, Ottawa, ON, 2015.
- [37] M. D. Takahashi, "A Flight-Dynamic Helicopter Mathematical Model with a Single Flap-Lag Torsion Main Rotor," NASA, NASA Technical Memorandum 102267, 1990.
- [38] J. Sitaraman, I. Chopra and J. Baeder, "Validation of UH-60A Rotor Blade Aerodynamic Characteristics Using CFD," in *59th American Helicopter Society International Annual Forum*, Phoenix, AZ, May 6-8, 2003.

- [39] J. Blazek, "Computational Fluid Dynamics: Principles and Applications", Elsevier Science Ltd, United Kingdom, 2001.
- [40] D. H. Charles, "Two-Dimensional aerodynamic characteristics of the NACA0012 airfoil in the Langley 8-foot transonic pressure tunnel," NASA, NASA-TM-81927, 1981.
- [41] T. J. Poinso and S. K. Lele, "Boundary Conditions for Direct Simulations of Compressible Viscous Flows," *Journal of Computational Physics*, vol. 101, no. 1, pp. 104-129, 1992.
- [42] F. Richez, "Numerical analysis of dynamic stall for different helicopter rotor flight conditions," in *AHS International 73rd Annual Forum & Technology Display*, Fort Worth, TX, May 9-11, 2017.
- [43] M. Potsdam, H. Yeo and W. Johnson, "Rotor Airloads Prediction Using Loose Aerodynamic/Structural Coupling," *Journal of Aircraft*, vol. 43, no. 3, pp. 732-742, 2006.
- [44] W. G. Bousman, "Aerodynamic Characteristics of SC1095 and SC1094 R8 Airfoils," NASA, NASA/TP-2003-212265, 2003.
- [45] J. Totah, "A Critical Assessment of UH-60 Main Rotor Blade Airfoil Data", NASA, NASA Technical Memorandum 103985, 1993.

Appendix A: Fluent Input Files

This appendix contains input files used in Fluent. Sample user defined functions used for controlling the pitching motion of the airfoil in the constant freestream dynamic stall simulations (A.1) and controlling the unsteady inlet boundary condition in the unsteady freestream dynamic stall simulations (A.2) are included. The airfoil coordinate of SC1095 and SC1094 R8 are also included.

A.1 UDF for Constant Freestream dynamic stall simulation

```
#include "udf.h"

#define pi 3.141592653589793

DEFINE_ZONE_MOTION(rotor_motion,omega,axis,origin,velocity,time,dtime)
{
FILE *fp;                                /*declaring the file variable for output*/

real alpha, om_alpha, alpha_mean, alpha_amp, f, k, uinf, c, w, aoa, aor;
real t = CURRENT_TIME;

alpha_mean = -8*(pi/180);                /*mean incidence angle for the motion in rad (10 deg)*/
alpha_amp = -8*(pi/180);                /*amplitude angle for the motion in rad (pitching
10 deg)*/
k = 0.06620735;                          /*reduced frequency*/
uinf = 204;                              /*free stream velocity, M = 0.6*/
c = 1;                                    /*airfoil chord (1 m)*/

f = (k*uinf)/(pi*c);                    /*pitching frequency in Hz*/
w = 2*pi*f;                              /*angular-frequency in rad/s*/

alpha = alpha_mean+(alpha_amp*sin(w*t)); /*sinusoidal equation of motion*/
aoa = -1*alpha*(180/pi);                /*switch "alpha" from rad to deg for
output*/

*omega = w*alpha_amp*cos(w*t);          /*angular-velocity for the motion*/
om_alpha = w*t;                          /*the angle of rotation at each
time*/
aor = om_alpha*(180/pi);                 /*switch "om_alpha" from rad to deg
for output*/

fp = fopen("Angles.txt", "a");           /*open a file named "Angles" for data
output*/

fprintf(fp,"%10.4f %10.6f %10.4f %10.4f\n", time, *omega, aor, aoa);
fclose(fp);

return;
}
```

A.2 UDF for Unsteady Freestream Dynamic Stall Simulation

```
#include "udf.h"

#define pi 3.141592653589793

DEFINE_ZONE_MOTION(rotor_motion,omega,axis,origin,velocity,time,dttime)
{
    FILE *fp;

    real alpha, om_alpha, alpha_mean, alpha_amp, w, aor;
    float t, tn;

    t = RP_Get_Real("flow-time");

    w = 89.238845;

    tn = t - 0.042016806;

    alpha_mean = -8.5*(pi/180);
    alpha_amp = -13*(pi/180);

    alpha = alpha_mean + (alpha_amp*sin(w*tn+pi));
    aor = -1 * alpha*(180 / pi);

    *omega = w*alpha_amp*cos(w*tn+pi);

    om_alpha = w*tn;
    aor = om_alpha*(180 / pi);

    fp = fopen("Angles.txt", "a");

    fprintf(fp, "%10.5f %10.5f %10.5f %10.5f\n", t, *omega, aor, aor);
    fclose(fp);
}

DEFINE_PROFILE(unsteady_velocity, thread, position)
{
    face_t f;

    real U, U_mean, U_amp, w;
    float t;

    t = RP_Get_Real("flow-time");

    U_mean = 136;
    U_amp = 27.2;

    w = 89.238845;

    U = U_mean + (U_amp*sin((w*t)));
}
```

```
begin_f_loop(f, thread)
{
    F_PROFILE(f, thread, position) = U;
}
end_f_loop(f, thread)
}
```

A.3 SC1095 Airfoil Coordinates

Table A.1: SC1095 airfoil coordinates continued [44].

Upper surface		Lower surface	
x/c	y/c	x/c	y/c
0.00000	0.00000	0.00000	0.00000
0.00010	0.00147	0.00010	-0.00112
0.00081	0.00396	0.00081	-0.00322
0.00203	0.00626	0.00203	-0.00510
0.00407	0.00913	0.00407	-0.00757
0.00661	0.01215	0.00661	-0.01020
0.00915	0.01473	0.00915	-0.01236
0.01220	0.01748	0.01220	-0.01453
0.01830	0.02220	0.01830	-0.01798
0.02440	0.02608	0.02440	-0.02066
0.03050	0.02934	0.03050	-0.02293
0.03660	0.03208	0.03660	-0.02494
0.04271	0.03443	0.04271	-0.02669
0.05084	0.03707	0.05084	-0.02862
0.06101	0.03979	0.06101	-0.03048
0.07117	0.04205	0.07117	-0.03191
0.08134	0.04398	0.08134	-0.03304
0.09151	0.04562	0.09151	-0.03397
0.10168	0.04705	0.10168	-0.03476
0.11693	0.04885	0.11693	-0.03580
0.13218	0.05033	0.13218	-0.03666
0.14743	0.05158	0.14743	-0.03737
0.16268	0.05265	0.16268	-0.03795
0.17794	0.05354	0.17794	-0.03841
0.19319	0.05426	0.19319	-0.03876
0.20844	0.05480	0.20844	-0.03903
0.22369	0.05518	0.22369	-0.03923
0.23894	0.05541	0.23894	-0.03935
0.25419	0.05553	0.25419	-0.03941
0.26945	0.05554	0.26945	-0.03941
0.28470	0.05547	0.28470	-0.03937
0.30503	0.05528	0.30503	-0.03924
0.32537	0.05498	0.32537	-0.03903
0.34570	0.05458	0.34570	-0.03874
0.36604	0.05407	0.36604	-0.03839
0.38638	0.05348	0.38638	-0.03797
0.40671	0.05280	0.40671	-0.03749
0.42705	0.05203	0.42705	-0.03695
0.44738	0.05118	0.44738	-0.03635
0.46772	0.05024	0.46772	-0.03569
0.48805	0.04922	0.48805	-0.03497
0.50839	0.04812	0.50839	-0.03419
0.52872	0.04694	0.52872	-0.03335
0.54906	0.04568	0.54906	-0.03245
0.56940	0.04434	0.56940	-0.03149
0.58973	0.04291	0.58973	-0.03047
0.61007	0.04140	0.61007	-0.02938
0.63040	0.03982	0.63040	-0.02824

Table A.2: SC1095 airfoil coordinates concluded [44].

Upper surface		Lower surface	
x/c	y/c	x/c	y/c
0.65074	0.03815	0.65074	-0.02703
0.67107	0.03640	0.67107	-0.02577
0.69141	0.03458	0.69141	-0.02445
0.71174	0.03267	0.71174	-0.02308
0.73208	0.03070	0.73208	-0.02166
0.75242	0.02865	0.75242	-0.02019
0.77275	0.02655	0.77275	-0.01868
0.79309	0.02439	0.79309	-0.01714
0.81342	0.02218	0.81342	-0.01557
0.83376	0.01993	0.83376	-0.01397
0.85409	0.01764	0.85409	-0.01236
0.87443	0.01532	0.87443	-0.01072
0.89476	0.01297	0.89476	-0.00908
0.91510	0.01060	0.91510	-0.00742
0.92527	0.00939	0.92527	-0.00659
0.93544	0.00818	0.93544	-0.00575
0.94560	0.00695	0.94560	-0.00489
0.95577	0.00570	0.95577	-0.00402
0.96594	0.00443	0.96594	-0.00313
0.97611	0.00360	0.97611	-0.00271
0.98627	0.00281	0.98627	-0.00229
0.99644	0.00201	0.99644	-0.00188
1.00000	0.00173	1.00000	-0.00173

A.4 SC1094 R8 Airfoil Coordinates

Table A.3: SC1094 R8 airfoil coordinates continued [44].

Upper surface		Lower surface	
x/c	y/c	x/c	y/c
0.00000	0.00000	0.00000	0.00000
0.00013	0.00185	0.00007	-0.00180
0.00090	0.00559	0.00072	-0.00501
0.00218	0.00945	0.00188	-0.00773
0.00427	0.01398	0.00384	-0.01053
0.00686	0.01825	0.00632	-0.01277
0.00944	0.02174	0.00881	-0.01419
0.01252	0.02532	0.01181	-0.01540
0.01867	0.03126	0.01783	-0.01702
0.02245	0.03441	0.02154	-0.01773
0.02857	0.03890	0.02757	-0.01872
0.03468	0.04264	0.03360	-0.01953
0.04077	0.04576	0.03963	-0.02017
0.04686	0.04837	0.04566	-0.02070
0.05294	0.05058	0.05169	-0.02115
0.06104	0.05306	0.05974	-0.02166
0.07115	0.05558	0.06980	-0.02218
0.08125	0.05764	0.07986	-0.02260
0.09135	0.05937	0.08992	-0.02294
0.10145	0.06083	0.09998	-0.02323
0.11154	0.06206	0.11005	-0.02348
0.12666	0.06359	0.12514	-0.02379
0.14179	0.06479	0.14024	-0.02406
0.15691	0.06576	0.15534	-0.02432
0.17202	0.06656	0.17044	-0.02459
0.18714	0.06718	0.18554	-0.02485
0.20225	0.06762	0.20063	-0.02512
0.21735	0.06790	0.21573	-0.02538
0.23246	0.06801	0.23083	-0.02564
0.24756	0.06798	0.24593	-0.02591
0.26266	0.06783	0.26103	-0.02617
0.27776	0.06758	0.27612	-0.02643
0.29286	0.06725	0.29122	-0.02665
0.31298	0.06671	0.31136	-0.02687
0.33311	0.06606	0.33149	-0.02701
0.35323	0.06531	0.35163	-0.02708
0.37336	0.06446	0.37176	-0.02709
0.39348	0.06352	0.39190	-0.02702
0.41360	0.06250	0.41204	-0.02690
0.43371	0.06139	0.43218	-0.02671
0.45383	0.06019	0.45232	-0.02647
0.47394	0.05892	0.47246	-0.02616
0.49406	0.05756	0.49261	-0.02580
0.51417	0.05612	0.51275	-0.02537
0.53428	0.05460	0.53290	-0.02489

Table A.4: SC1094 R8 airfoil coordinates concluded [44].

Upper surface		Lower surface	
x/c	y/c	x/c	y/c
0.55439	0.05300	0.55304	-0.02435
0.57450	0.05132	0.57319	-0.02375
0.59460	0.04955	0.59334	-0.02309
0.61471	0.04771	0.61349	-0.02237
0.63481	0.04579	0.63364	-0.02159
0.65491	0.04379	0.65379	-0.02075
0.67501	0.04171	0.67394	-0.01985
0.69511	0.03955	0.69409	-0.01889
0.71521	0.03732	0.71425	-0.01788
0.73531	0.03501	0.73440	-0.01682
0.75540	0.03263	0.75456	-0.01572
0.77550	0.03020	0.77472	-0.01458
0.79559	0.02771	0.79487	-0.01340
0.81568	0.02518	0.81503	-0.01220
0.83577	0.02260	0.83519	-0.01097
0.85587	0.01998	0.85535	-0.00972
0.87596	0.01733	0.87551	-0.00845
0.89605	0.01466	0.89567	-0.00718
0.91614	0.01195	0.91583	-0.00589
0.92618	0.01059	0.92591	-0.00524
0.93623	0.00921	0.93599	-0.00458
0.94627	0.00782	0.94607	-0.00390
0.95631	0.00641	0.95615	-0.00322
0.96636	0.00498	0.96623	-0.00251
0.97641	0.00398	0.97630	-0.00227
0.98646	0.00301	0.98637	-0.00203
0.99651	0.00205	0.99644	-0.00180
1.00000	0.00171	1.00000	-0.00171

Appendix B: Blade Geometry Used in Qoptr

This appendix shows the modelling of the UH-60A rotor blade geometry for use in Qoptr. All information used for the modelling of blade geometry was obtained from Ref. [45]. Pitch, chord, and airfoil distribution are shown, respectively.

B.1 Pitch Distribution

Table B.1: UH-60A main rotor blade pitch distribution.

r/R	Theta (r) [deg]
0	9.65
0.18	9.7
0.219	9.37
0.292	8.06
0.463	5.057
0.498	3.458
0.541	2.71
0.689	0.0324
0.746	-0.9531
0.778	-1.422
0.825	-1.891
0.852	-1.136
0.871	-1.277
0.924	-3.485
0.935	-3.579
0.951	-3.484
0.958	-3.061
0.972	-2.542
0.986	-1.79
1	-1.318

B.2 Chord Distribution

Table B.2: UH-60A main rotor blade chord distribution.

r/R	Chord (r) [c/C]
0	1
0.15	1
0.46	1
0.496	1.01
0.73	1.01
0.735	1.075
0.863	1.075
0.864	1
0.865	1.064
1	1.064

B.3 Airfoil Distribution

Table B.3: UH-60A main rotor blade airfoil distribution.

r/R	Airfoil (r)
0	SC1095
0.47	SC1095
0.5	SC1094 R8
0.82	SC1094 R8
0.85	SC1095
1	SC1095